AO and MICADO: Impact on Astrometry

Issue	*1.0*
Release Date	*26.02.2014*
Authors	*Remko Stuik, Gijs Verdoes Kleijn, Koen Kuijken, Eline Tolstoy, Tibor Agocs and John McFarland*
Released	*Ramon Navarro*

Executive Summary

The relative astrometric accuracy of MICADO is required to be better than 50 micro arcseconds relative over the FoV. This means that the contribution of the ADC must be less than 10 micro arcseconds, while the atmospheric dispersion over the observed band reaches 0.5 arcseconds and the absolute atmospheric refraction reaches 20 arcseconds. The performance of the MICADO ADC was not studied during the MICADO Phase A study.

An initial study on the impact of the ADC on the astrometric performance of MICADO [1] identified several issues in the design of the ADC, which we tried to address in this follow-up study. In order to identify cross correlation effects, also the effects of the atmosphere, Telescope, Adaptive Optics, SCAO system, MICADO, the detector and the data reduction software algorithms are taken into account. In particular, we extended the initial study in several areas:

- A more extensive set of types of ADCs were studied and detailed investigations, including first-order tolerancing and costing were done.
- For all ADCs the astrometric performance was re-evaluated.

- A first start was made for a full end-to-end astrometric simulator. Currently this is limited to a combination of AO and ADC, but as more information becomes available, the simulator will be extended.
- A first-order astrometric pipeline was developed in order to assess both the challenges in an astrometric pipeline as well as to characterize the results from the simulator.

Our intention was to study the effects of the MAORY multi conjugate adaptive optics system, the impact of telescope vibrations and distortions due to the MICADO optics. Unfortunately none of the input parameters required for this part of the study became available. We were able to interact with LESIA, currently leading the SCAO efforts, and were able to obtain a (limited) set of SCAO simulation data near the end of our study. Although we would have liked to be able to spend more time on these simulations and could have used simulations over a wider range of parameters. We can still draw conclusions on the use of SCAO for astrometry.

At this moment we have two ADC designs that do not interfere with the ability to carry out accurate astrometry: a counter rotating ADC in the SCAO pupil plane and a linear ADC just before the MICADO image mask plane. Both types of ADCs can be made using existing blanks and manufacturing techniques, although another tolerancing round and discussion with manufacturers will be required. Each of these two ADCs has its advantages and disadvantages and a selection can only be made taking into account the boundary conditions given by the full MICADO instrument. Using the SCAO simulations, we have not found any showstoppers for accurate astrometry with MICADO and the E-ELT, although the exposure times needed to reach the current requirements are longer than currently desired.

Table of Contents

1 Scope and requirements

This study was triggered by the requirement to make an accurate estimate of the manpower requirements, cost and feasibility of NOVA building the Atmospheric Dispersion Corrector (ADC) for MICADO and to understand the impact of the technical trade-offs on the likely scientific performance. Here we investigated:

- The requirements and feasibility of specific ADC designs
- The impact of the choices on the required accuracy of the ADC
- The potential assistance from software.
- To be able to make an accurate proposal to NOVA and to the MICADO consortium to build an ADC

Our performance targets are mainly driven by the exacting requirements for accurate astrometry:

“For an unresolved, unconfused source of optimal brightness in the centre of the field of view the relative position on the sky with respect to an optimal set of reference sources must be reproducible to within 50 µas (goal: 10 µas) over all timescales in the range of 1 hour to 5 years.”

During this study it became clear that the final design of the Multi-Conjugate AO system, MAORY, is not yet decided, and thus it is currently not possible to consider it to be a driver for the design of the MICADO ADC. This study has therefore concentrated on MICADO operating with the SCAO relay. This has an impact on the science that can be done (see section 2), the field of view over which accurate astrometry is feasible (see section 3) and the locations where an ADC could be physically placed.

Furthermore, only a limited optical model was available at the time of the simulations. This means that we could only investigate the relative impact of the ADC on the optical quality, but not the impact of instrumental distortions.

Lastly, although we found a clear solution for the best ADC for optimum astrometric performance, other factors may make this rather hard to implement, and in the end the likely performance of both ADCs are fairly similar. Further hard requirements are required by the second-most demanding application, which is coronagraphy. This requires a fixed orientation of the pupil with respect to the camera (i.e., the ADC should not change the relative rotation of the pupil); a pupil stability that is better than 0.5% PtV; residual chromatic errors should be <0.3 mas over a small field (Nx lambda/D) and the ADC should not cause image displacements at similar level. Note that in order to achieve the last requirement, an active feedback system might be required. Finally, any ADC positioned up-stream from the AO wavefront sensor should have a good transmission over the wavelength range 450-720 nm. This required a change in glass types from the initial ADC study.

Initially we hoped to allow for an alternate solution with two smaller ADCs (one for coronagraphy, one for astrometry), however, complications both from the cooling of such an ADC as well as from managing a moving object within MICADO removed this option from consideration at an early stage.

2 Science

There are three key capabilities that exemplify the unique features of MICADO at the E-ELT and that will contribute to make it the most powerful optical/infrared instrument available until a telescope with a larger aperture is built. These capabilities lie at the heart of the primary science cases that have driven the design of the camera, and they are:

- Sensitivity and Resolution
- Precision Astrometry
- High Throughput Spectroscopy

These key capabilities will yield new insights into the structure and physics of numerous objects of astrophysical interest and allow the discovery and study of many new and/or unexplored phenomena. This superb astrometric precision means that astronomical sources need no longer be static but become dynamic. Historical examples demonstrate that attaining dramatic new additional capabilities leads to breakthroughs. In this case we expect to expand our understanding of the three dimensional structure and evolution of a range of targets. Spectroscopy over a long wavelength range has also been shown to be a very powerful diagnostic (e.g., X-shooter on the VLT), especially for the discovery and characterization of new sources over a range of red-shift and also to cover different types of sources (from stars, Supernovae explosions and GRBs to galaxies).

A fundamental requirement for all these capabilities is a well understood and well behaved point spread function. The planned adaptive optics modules make the fundamental corrections required for the atmospheric conditions, but an ADC is also required to correct for the wavelength dependent refractive index of air. The ADC will be needed for all broad-band observations which require optimum sensitivity and spatial resolution. The capability most affected by the functioning of the AO and the ADC is the precision astrometry.

It now seems likely that MICADO will operate for the first years using its own internal SCAO module. This was an executive decision by ESO. Thus the SCAO module is currently the only AO option that is sufficiently well defined for us to be able to design an ADC. The SCAO mode makes astrometry (and photometry) somewhat more challenging than the MCAO module, but it is also easier to predict how it will work and interact with the ADC, as this is a more standard and simple form of AO correction. It is also very convenient that the SCAO module is part of the MICADO instrument and the group building it is part of the MICADO team.

The SCAO mode produces a higher Strehl Ratio than the MCAO system, and so it has always been the ideal tool for studies of the central regions of (active) galaxies, including but not restricted to the Galactic centre. Also the gravitational lensing science case may prefer to use SCAO, as it is typically concerned with very small spatial scales, and does not require a large field of view. The only science cases which will most likely have to wait for an MCAO system is the wide-field astrometry cases looking at nearby galaxies and globular clusters and deep imaging of blank sky fields looking for high redshift objects. However, even with SCAO the small and compact central regions of globular clusters can still be accurately monitored for astrometric studies. Likewise the detailed imaging of individual (known) high redshift galaxies may prefer SCAO because they don't need a large field of view and they would also benefit from the increased Strehl Ratio.

Thus the change of strategy coming from ESO, to delay the MCAO module, does not significantly hamper the Dutch scientific plans for MICADO. In fact it makes it easier to develop the scientific program in stages, starting with the simpler small-field approach before going to the large field of view.

3 Impact of Adaptive Optics on astrometry

Based on earlier discussions and write-ups by Trippe, Ellerbroek and others, we can identify properties of Adaptive Optics that impact the astrometry:

1. The overall tip-tilt stability is dominated by the ground layer and vibrations of the telescope. There are two effects; the PSF is blurred by the given TT-stability and the actual position of stars is perturbed. The latter is less important for relative astrometry, as all stars in the field undergo the same tip-tilt motion. The blurring of the star means that the PSF of the star is effectively convoluted with a blur with a FWHM of several mas. The exact shape of this blur depends heavily on the time scales of the TT-jitter and the exposure time. For METIS, the overall RMS tip-tilt fluctuations, based only on stochastical AO simulations, are estimated to be of the order of 5 mas. For MICADO, the requirements will be significantly stronger and driven by the coronagraph (0.3 mas).
2. The long term stability of TT-signal does not deviate significantly from this number. The stability is given by the stability of the loop and as long as the loop remains closed, TT-residuals might scale with external factors, but variations will be small. Outside this range, the observing conditions have deteriorated so much that in practice the observation will be stopped. Considering this, and that these residuals are random, a SQRT(t) decrease in position and a fixed value of <5 mas in blurring can be assumed, also on longer time scales.
3. MCAO relies on several stars (~3) in the field for lower order mode correction. Individual stars have a stability as described above, but for relative astrometry, it is the relative stability of these stars as a function of time. This requires a separation between correlated motions and uncorrelated motions. The first relate directly to motions induces by the ground layer turbulence plus vibrations, while the latter relate to higher-layer turbulence. In strength, the separation is of the order of ~90% common motion and ~10% non-common motions. Using the number above, the relative motions of the guide stars will leave uncorrected scale variation of the order of 500 micro-arcseconds over the 1 arcmin field of view. This scale factor will average out as a function of time, with SQRT(t), but will leave a position dependent blurring of the PSF, varying between 0 at the weighted center of the guide stars, and up to 250-500 micro-arcseconds at the edge of the field of view. The blurring is non-symmetric, but aimed at the center of the weighted center of the guide stars. For the SCAO system this is not an error sources.
4. Stability of the Laser Guide Star Tomography – probably can be included into PSF stability. For the SCAO system, this is not an error source.
5. PSF centroiding stability falls into two categories; the accuracy with which the centroid of a specific PSF can be determined and the impact of the halo of the surrounding PSFs on the centroiding accuracy. The centroid of the PSF depends on the instantaneous distribution of the turbulence in the atmosphere, as compared to the correcting elements, i.e. the 3 DMs for MCAO and 1 DM for SCAO. If the atmospheric profile would be stable, the temporal fluctuations on the PSF shapes will average out as SQRT(t) and is only dependent on the position. With a varying atmospheric profile, the PSF will only stabilize as SQRT(N), where N is the number of independent configurations of the atmosphere. In practice there will only be a few realizations of N during an exposure, which means that the PSF will not stabilize. The only way to solve this is

by very careful calibration of the PSF, or might be determined by PSF reconstruction based on WFS data. The latter might not include all cross-coupling effects, like ADC and drifts in the NCPA's.

6. Scintillation – In the classical regime, scintillation is mainly an intensity fluctuation, but using MCAO, scintillation might also introduce local plate scale variations. These variations are directly coupled to the instantaneous wavefront disturbances and should therefore, for exposures significantly longer than the crossing time of turbulence (~1-2 seconds) decrease with SQRT(t). The initial magnitude of the effect needs to be investigated, but expected to be small with respect to, for example, the plate scale variations due to the positioning inaccuracies of the natural guide stars. For now these are neglected. For SCAO, this term does not exist, although relative intensity fluctuations might lead to variations in the centroiding.
7. Orientation of the field between exposures will cause that some of these effects, that are in principle reproducible, will have different impacts for each observation. Keeping the orientation the same, i.e. observing at the same sidereal time, would allow for a reduction of some of the error terms.
8. Chromatic variations in the PSF. The AO correction is chromatic, in the sense that the atmospheric wavefront are chromatic, while the corrections are not. The residuals are therefore chromatic and cause a wavelength dependent PSF. This chromatic variation can change as a function of space and time.
9. Mixing terms with other (astrometric) effects?
    a. The guide stars will be at different Altitudes, each having a different atmospheric refraction. Since the guide stars are part of the same reference grid as the stars for which you want to know the position, this linear term of this effect is already taken into account. But since the AO system performs a linear interpolation between its guide stars, any higher order terms in the atmospheric refraction are not accounted for. It is currently unclear at what level this effect will play a role.
    b. More?

From the above, it should be concluded that the main issues are in the determination of the center of the PSF under varying atmospheric conditions and in varying positions in the field. Some of the detrimental effects of not being able to do a full simulation can be mitigated by careful studying of the PSF calibration.

Furthermore, several of the above effects also come into play for SCAO systems, for which we do have the tools to run simulations. Considering the complexities of the MCAO system, it is also conceivable that MICADO will run several years with only the SCAO system operational. Running SCAO simulations now has the added benefit that it will allow for assessing the availability of high-precision astrometry in the first few years of MICADO.

The differences in correction between SCAO and MCAO impacts astrometry in two areas; 1) the Point Spread Function (PSF) will vary significant over the field of view. This will severely impact the centroiding and 2) the correction is only performed in a single direction, which can cause unsensed plate scale variations, local and global, over the field of view, which can be expected to be stronger at larger distances from the guide star. The latter is seen in the SCAO simulations which we analyzed in Section 5.2.

3.1 Quick analysis of MAD data

Koen Kuijken ran a quick analysis of existing MAD data from the VLT. These data consisted of a series of 20 exposures, 10 seconds each, in K band, over a time span of 1.5hrs (2008-08-16T01:18:22 to 2008-08-16T02:40:48). The images contain the outer regions of globular cluster NGC 6441, a dense star field. Each MAD image is ~50 arcseconds square, and 2048x2048 pixels with a scale of 28 mas/pix. See Figure 1. The dithers between exposures extend over more than 200 pixels. Stars in the images have a Gaussian FWHM of about 5 pixels. These images were not taken with the aim of carrying out astrometry.

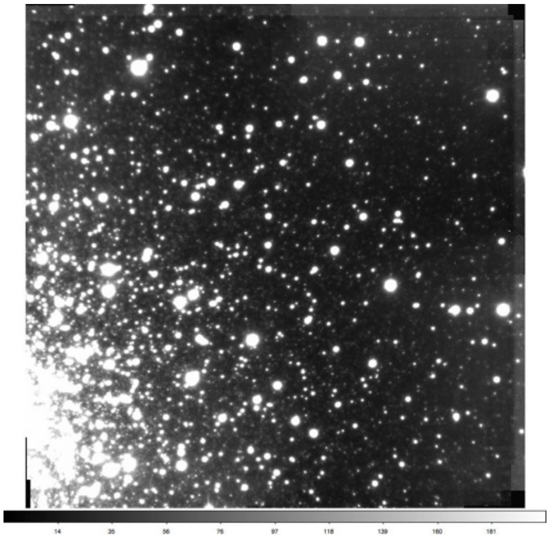

Figure 1. Test image of the outer region of globular cluster NGC6441, which was used to estimate astrometric accuracy of the MCAO imager, MAD on the VLT.

The analysis carried out was similar to what was done previously with HST images (eg Kuijken & Rich 2002 AJ 124, 2054). It works by determining the pixel position of all the stars in each exposure by PSF fitting (in this case a 'shapelet'=gaussian*polynomial model is used), and then to astrometrically map the fields to a common reference system using polynomial distortion maps. This process is iterated with 3-sigma clipping to remove outliers. For this analysis only the ~250 brightest stars in the image were used, and excluding the crowded corner near the center of the star cluster. All stars measured stars were given equal weight.

Figure 2 shows the results of this analysis, for distortion models of increasing complexity (from linear = 3 coefficients to 4th order polynomial = 15 coefficients). Note that each exposure gets its own distortion model, and no assumption about temporal stability is made: only the stars in the field are used as the calibrators. Each panel shows the rms position dispersion after 3-sigma clipping: every point is a different individual star, and the plotted dispersion is the RMS of the 20 remapped positions. The curve is the same in each plots, and shows the 1/sqrt(flux) dependence that would be expected from pure photon noise.

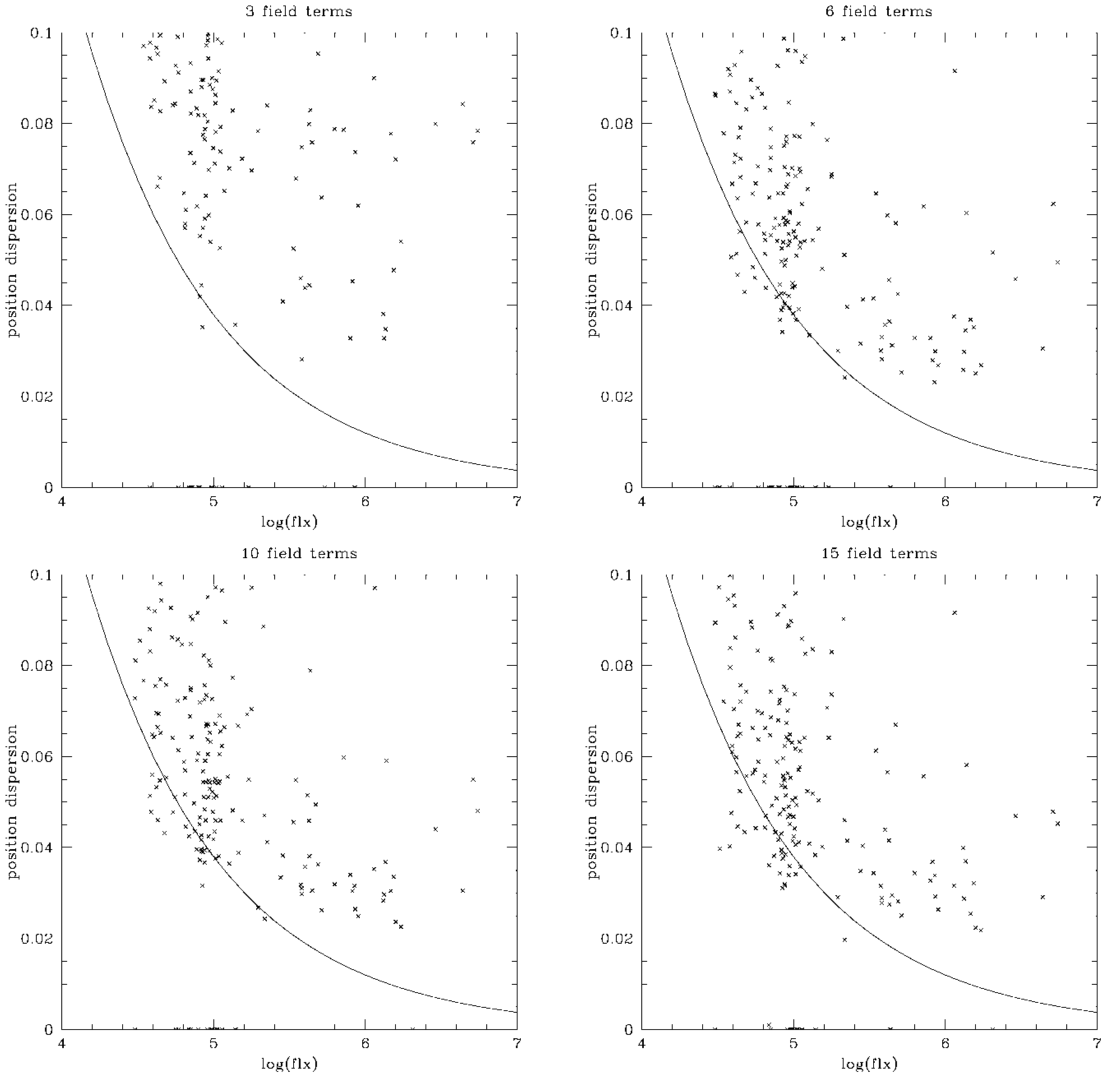

Figure 2. Results of the astrometric analysis of a sequence of VLT/MAD images, like those shown in Figure 1, for increasing order of a polynomial fit of a distortion model.

It is clear that there is little difference between the cubic and quartic distortion models. A 'floor' of about 0.03pix rms is evident. Even the rms of the brighter stars does not fall below this level. The reasons for this floor could be manifold: e.g. pixel sampling effects (although unlikely for these very well resolved stars), atmospheric dispersion (MAD had no ADC), or high-order field distortion terms induced by the AO. All this would need to be investigated by correlating the residuals against pixel phase, color, distance from the guide stars, etc. But this relatively straightforward analysis already shows that it is possible to achieve an rms position of .03 pixel with these data, which is 850 micro-arcseconds, with a single 10-sec exposure with an MCAO system on the VLT. How this will average down can only be demonstrated with multi-epoch observations, but with properly dithered data it will: so 850 micro-arcseconds is likely to be a very conservative upper limit of what can finally be achieved. The residual error maps are shown in Figure 3.

Simple scaling of these results to the pixel scale of MICADO, i.e. 3 mas leads to an rms astrometric precision of ~100microarcsec accuracy.

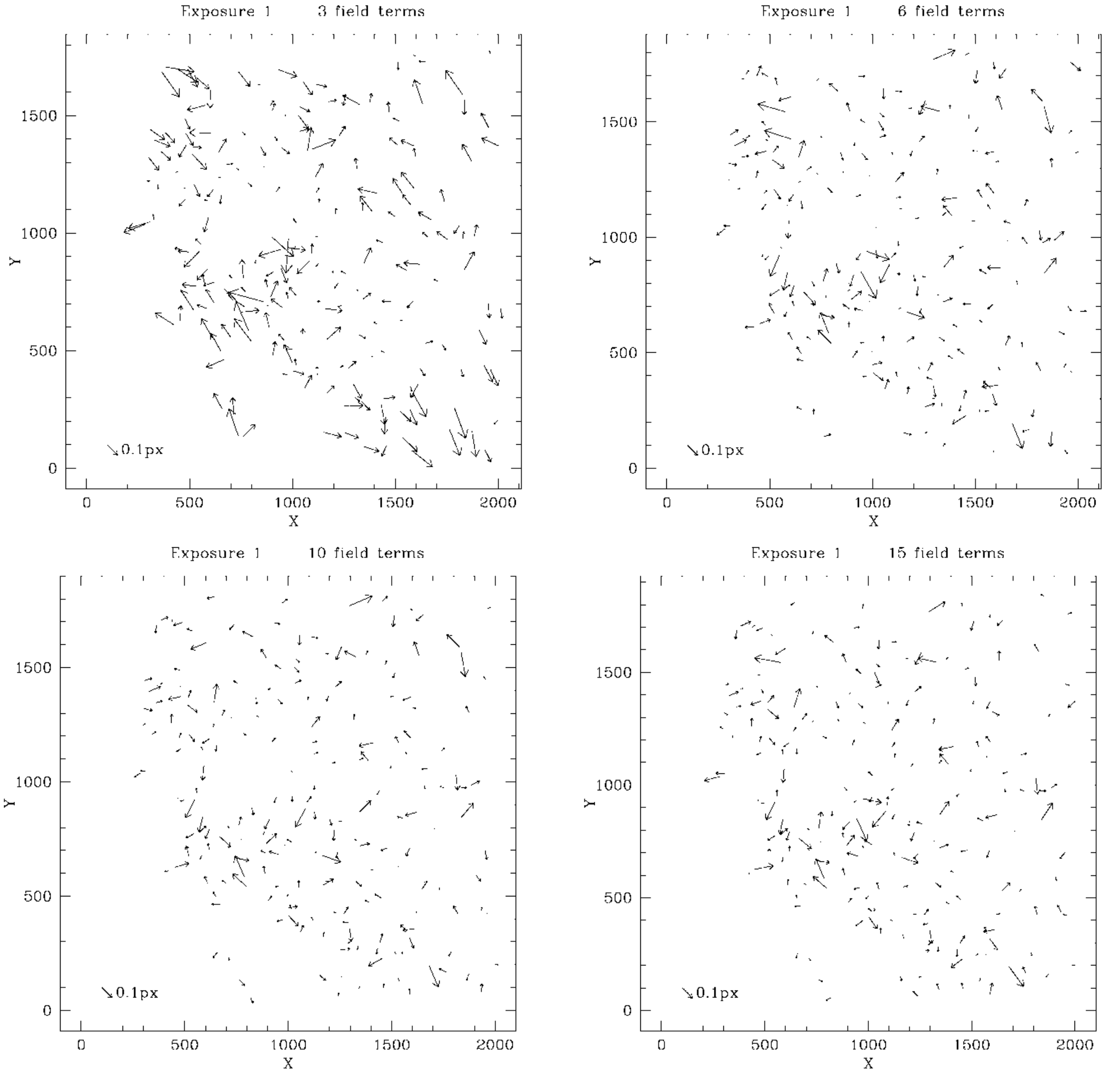

Figure 3. Three example residual error maps for the various polynomial distortion models from the results shown in Figure 2. No immediate correlation can be seen with a 3-guide-star configuration, but further work needs to be done on this.

4 ADC Designs and trade-off

4.1 Introduction

The aim of this study is to investigate the different ADC configurations for the (SCAO-)MICADO system and bring the analysis to a level where the performance, tolerances and cost of the ADC can be evaluated against several aspects of the science operation of MICADO.

In the previous phase of the project a short study was done, in which we compared two types of counter-rotating ADCs:

- The ADC as described in the MICADO Phase A Opto-Mechanical design. This is a set of counter-rotating prisms made up of ZnSe/ZnS. This ADC is located ~450 mm before the focus (of the telescope). In order to correct the optical errors caused by locating the ADC close to the image plane, two of the surfaces of the ADC have a small cylindrical curvature (~500 meter).
- A similar set of ZnSe/ZnS counter rotating prisms located in a pupil plane of the MCAO system before MICADO, with the angles optimized for performance over 0.58 -2.50 micrometers.

The result of the study showed that the counter-rotating pupil plane ADC was performing much better than the focal plane ADC. In the continuation of the previous phase several additional ADCs were investigated both in the focal plane of MICADO and pupil plane of the SCAO/MCAO systems. We identified and investigated two ADC types:

1. Counter rotation based designs (already mentioned before). Two counter rotating prism pairs introduce the necessary dispersion. This type of ADCs can be placed in the pupil plane or in the focal plane of the optical system.

2. Linear ADC. Two prisms with varying separation between them produce the necessary dispersion. This type of ADC works only in the vicinity of the focal plane.

For both of these designs we look at zero-deviation versions, which means that we intend to find solutions, where the optical axis displacement or tilt is minimized.

In section 4.1.1, focal plane ADCs are investigated and trade-off between them is presented. Section 4.3 describes the two best ADC designs: a linear ADC in the focal plane of MICADO (selected from the designs showed in section 4.1.1) and a counter rotation based ADC in the pupil plane of the SCAO system. Many other designs were investigated, but not shown in the following. They were eliminated on the basis of the following criteria:

- unacceptable chromatic spread of the PSF (residual dispersion)
- the insufficient pupil performance inside MICADO
- problematic ADC materials (transmission, manufacturability)

4.1.1 Astrometric performance of the ADCs

For each of the Zenith angles and bands, the distance is furthermore measured between 8 points in the field of view of MICADO. For the first part of this study, these points were taken at the edge of the field of view of MICADO and in the image center, while in the detailed investigation, the points were taken on a square with sides of 10” around the center of the field of view. The smaller field was chosen to be compatible with the change from computations for a MCAO system to a SCAO system.

The results are compared with respect to the distance measured at Zenith. The residuals are considered the astrometric offsets. The results are plotted in two ways: The first shows the large scale structure of the astrometric offsets, and is shown in Figure 4, left. For an ideal ADC, these offsets can be either computed or calibrated with high accuracy and should not lead to an increase in the astrometric error, as long as interactions with other error terms are minimized. The second way is to zoom in on the lower left corner point for each zenith angle, see Figure 4, right, **Error! Reference source not found.** again, subtracting the average differential distance for each band. If the wavelength dependence of the intensity of the source is known, this still does not contribute to the astrometric error as this is still a deterministic error.

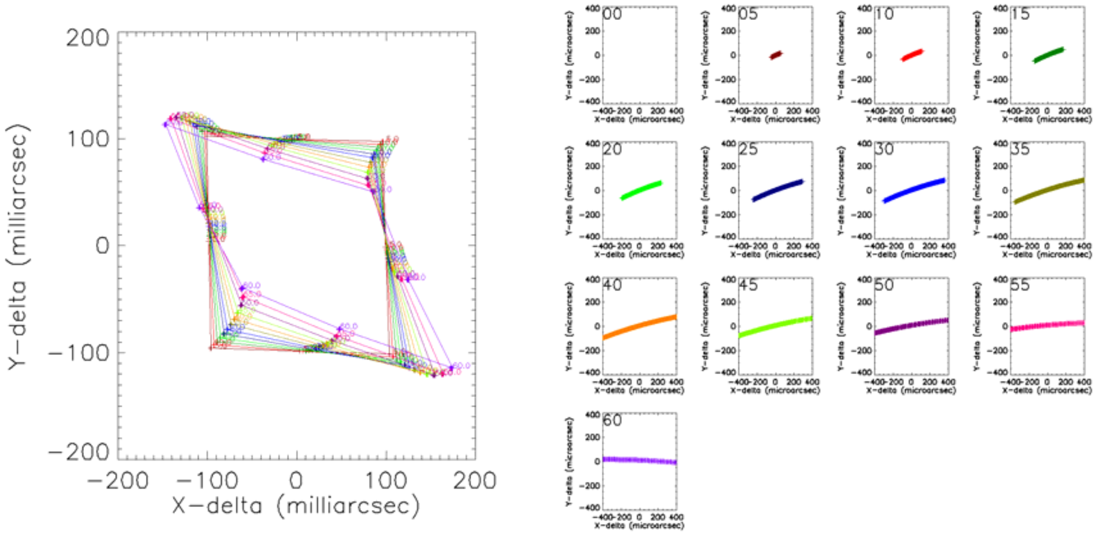

Figure 4. Zoom-in of the two type of figures which are used to compare the performances of the various ADC types. Both are double differences, i.e. the difference between zenith and given angle and the difference between the center of the field of view and given point. (left) shows the large scale structure of the astrometric distortions. For zenith, all points are plotted on a square and the difference with respect to this square is an indication of the residual astrometric error. (right) shows the residual chromatic errors, i.e. each point in each curve corresponds to a wavelength point within the corresponding band and the spread in the points corresponds to a residual chromatic error. Each panel corresponds to a different zenith angle, from 0 degrees in the upper left, in steps of 5 degrees, via 15 degrees in the upper right, to 60 degrees in the lower left. The angle is indicated in the upper left corner of each panel. Note that for each panel both the numerical value as well as the scale (milliarcseconds/microarcseconds) changes from panel to panel (although the scale will generally remain constant over wavelength bands for the same ADC).

4.2 Focal plane ADC-s investigated

In the following sub-section, six focal plane ADC-s are analyzed:

1. The original focal plane ADC that is detailed in the MICADO phase A document.
2. A counter rotation based ADC with a very good material combination (S-NPH2 and Spinel) to match the atmospheric dispersion in the 0.8-2.5 micron range.
3. Same as in point 2, but with zero deviation (meaning that there is no spot drift in the focal plane as the ADC rotates).
4. Linear ADC.
5. Same as in point 4, but with zero deviation (no spot drift in the focal plane as the linear ADC moves).
6. Linear ADC with fold mirror.

A 0.014°x 0.014° square field of view and 0.8-2.5 µm wavelength range was modelled for the analysis and optimization of the ADC-s. For all designs six figures are presented. In the first two figures the spot diagrams are shown (MICADO detector plane) for 0 degree and 65 degrees zenith angle. In the third figure the residual dispersion, in the forth the spot drift in the focal plane (or pupil tilt) are presented. Finally in the fifth and sixth figures the pupil shear are shown, first for one wavelength for different zenith angles (represented by different colors) and secondly for 65 zenith angle for different wavelength (represented by colors). In the Annex the RMS spot radius vs field and RMS spot radius vs wavelength are also included for the worst case 65 degree zenith angle configurations.

For the sake of comparison, in all designs the first optical surface is 565 mm before the focal plane (this was the location of the original phase A ADC). The most recent space envelope for the focal plane ADC is a 250mm wide volume 200mm before the focal plane. All the designs presented in the following can be accommodated for this space envelope, although for the linear ADC generally more space is needed and in some cases it can lead to difficulties (zero-deviation versions need more space).

For all designs telecentric and non-telecentric relays were both considered and analyzed. In most of the cases the results were the same. Situations, where the results were different are detailed in the specific sections.

4.2.1 Phase A focal plane ADC

In the following we look at the performance of the system using the original phase A design of the ADC. The materials are ZnSe and ZnS and the first and last optical surfaces are cylindrical.

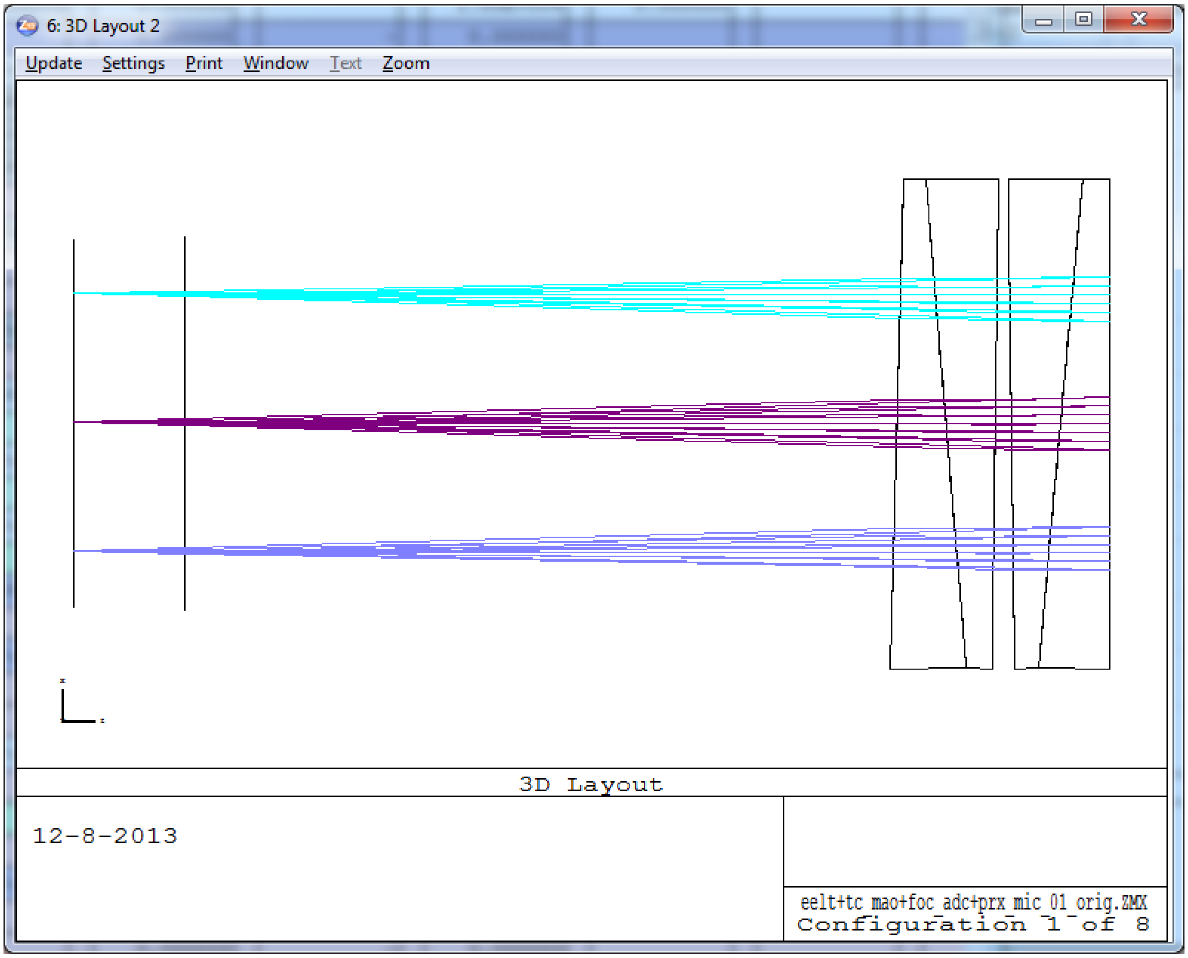

Figure 5 Layout of the phase A ADC. The focal plane with and without the ADC is also shown.

In the following the spot diagrams can be seen for 0 degree and 65 degrees zenith angle.

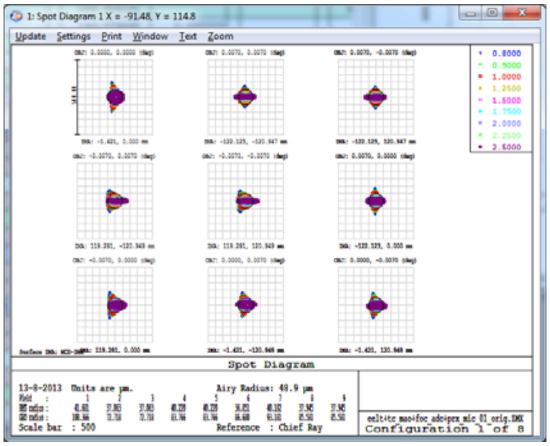

Figure 6 Spot diagrams for zenith (in the MICADO detector plane). Scale is 500 microns.

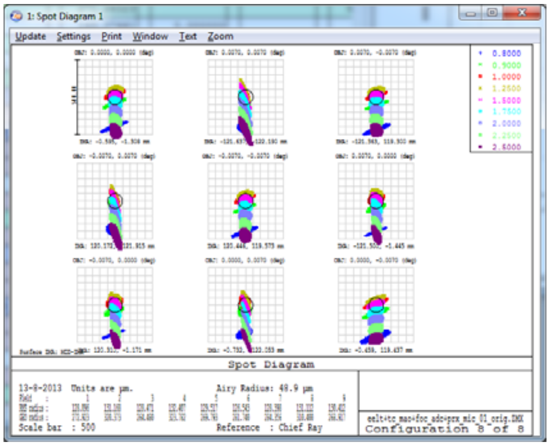

Figure 7 Spot diagrams for zenith angle 65 degrees. Scale is 500 microns.

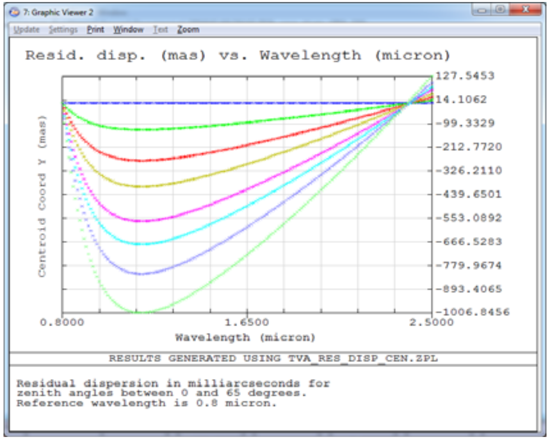

```
RESULTS GENERATED USING TVA_RES_DISP_CEN.ZPL

Residual dispersion in milliarcseconds for
zenith angles between 0 and 65 degrees.
Reference wavelength is 0.8 micron.
```

Figure 8 Residual dispersion in mas (PV is 1135 mas) for zenith angles 0, 15, 30, 40, 50, 55, 60 and 65 degrees.

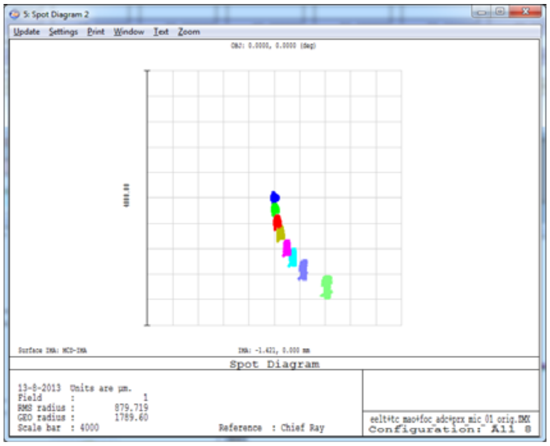

```
Surface IMA: MCD-IMA                IMA: -1.421, 0.000 mm
13-8-2013  Units are µm.
Field      :          1
RMS radius :    879.719
GEO radius :    1789.60
Scale bar  : 4000              Reference  : Chief Ray
eelt+tc mao+foc adc+prx mic 01 orig.ZMX
Configuration: All 8
```

Figure 9 Spot drift is around 4mm as the ADC rotates. Spots for zenith angles 0, 15, 30, 40, 50, 55, 60 and 65 degrees are shown.

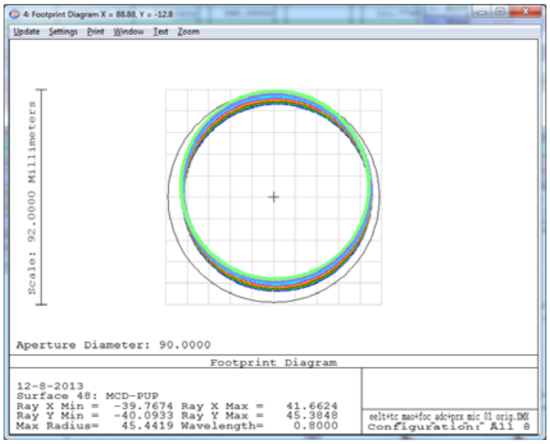

```
Aperture Diameter: 90.0000

12-8-2013
Surface 48: MCD-PUP
Ray X Min =  -39.7674 Ray X Max =   41.6624
Ray Y Min =  -40.0933 Ray Y Max =   45.3848
Max Radius=   45.4419 Wavelength=    0.8000
eelt+tc mao+foc adc+prx mic 01 orig.ZMX
Configuration: All 8
```

Figure 10 Pupil shear for 0.8 micron wavelength. The colors represent different zenith angles.

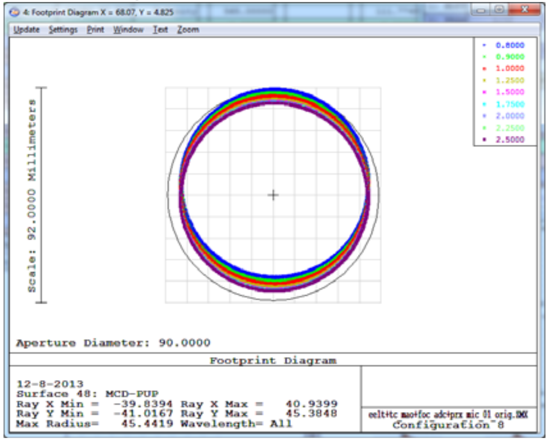

```
Aperture Diameter: 90.0000

12-8-2013
Surface 48: MCD-PUP
Ray X Min =  -39.8394 Ray X Max =   40.9399
Ray Y Min =  -41.0167 Ray Y Max =   45.3848
Max Radius=   45.4419 Wavelength= All
eelt+tc mao+foc adc+prx mic 01 orig.ZMX
Configuration 8
```

Figure 11 Pupil shear for 65 degrees zenith angle. The colors represent wavelengths between 0.8-2.5 micron.

The non-telecentric relay has two effects on the phase A ADC. The residual dispersion and the chromatic pupil shift decreases. This is understandable since the phase A ADC was designed for a non-telecentric MAORY. The residual dispersion and the pupil shift for one wavelength can be seen in the following figures.

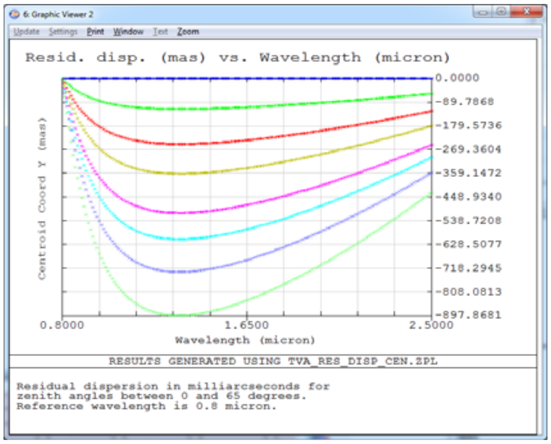

```
RESULTS GENERATED USING TVA_RES_DISP_CEN.ZPL

Residual dispersion in milliarcseconds for
zenith angles between 0 and 65 degrees.
Reference wavelength is 0.8 micron.
```

Figure 12 Residual dispersion in mas (PV is 898 mas) for the zenith angles 0, 15, 30, 40, 50, 55, 60 and 65 degrees.

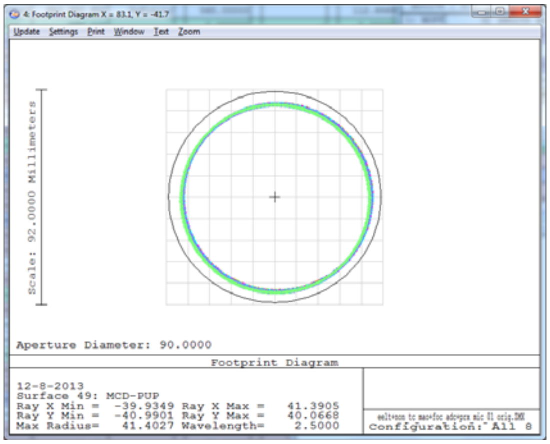

```
Aperture Diameter: 90.0000
Footprint Diagram
12-8-2013
Surface 49: MCD-PUP
Ray X Min =  -39.9349 Ray X Max =   41.3905
Ray Y Min =  -40.9901 Ray Y Max =   40.0668
Max Radius=   41.4027 Wavelength=    2.5000
Configuration: All 8
```

Figure 13 Pupil shear for 0.8 micron wavelength. The pupil quality is similarly good for all wavelength. (The colors represent different zenith angles.)

4.2.2 Counter rotation based ADC (based on S-NPH2 and Spinel)

In the following a counter rotation based ADC is investigated, which consists of materials S-NPH2 and SPINEL. This material combination was found in literature [1] as the best that compensates atmospheric dispersion in a very similar wavelength range required. Similarly to the previous section, the spot radii, residual dispersion, pupil shear and spot drift in the focal plane (pupil tilt) are shown. This ADC is very similar to the phase A ADC, but it only contains flat surfaces.

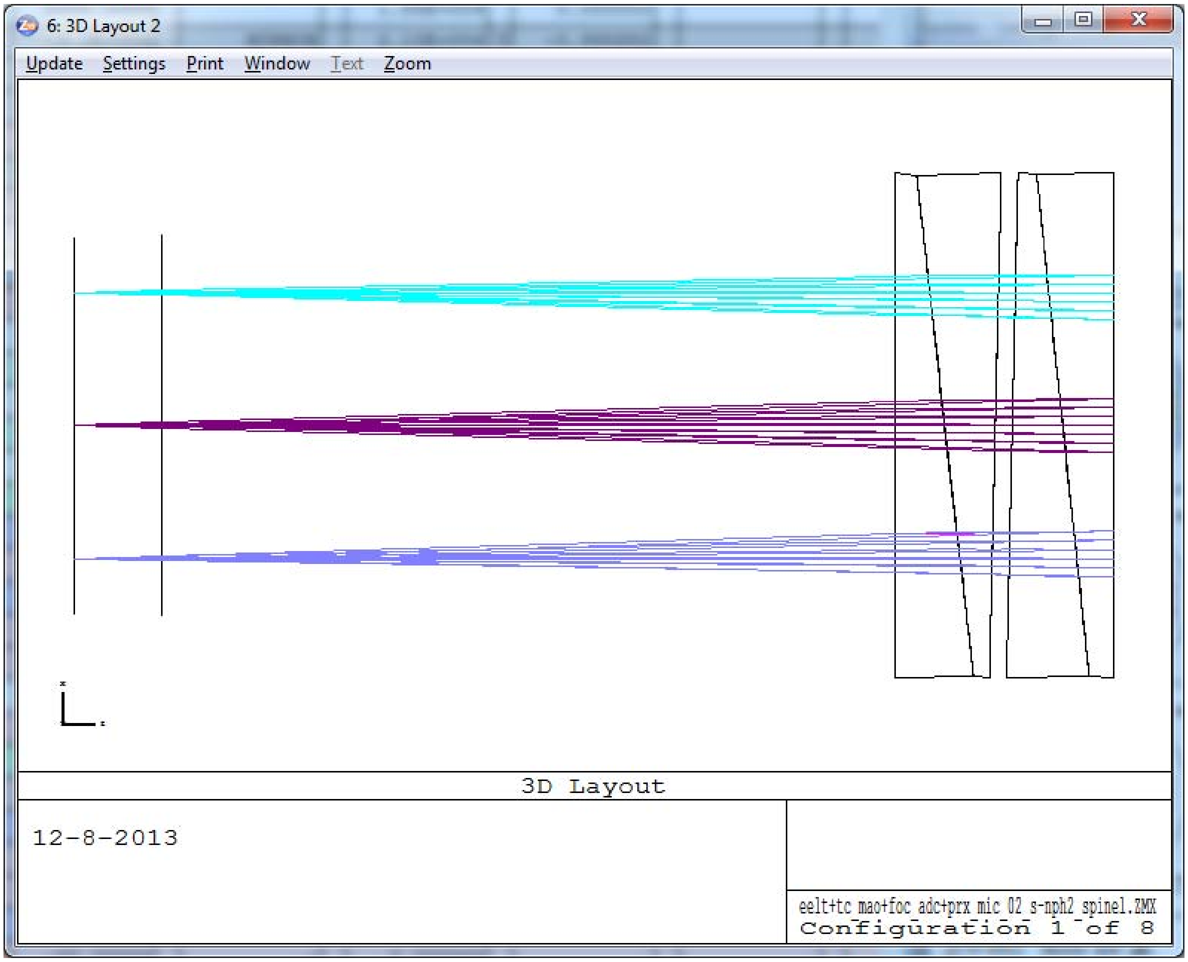

Figure 14 Layout of the counter rotation based ADC. The focal plane with and without the ADC is also shown.

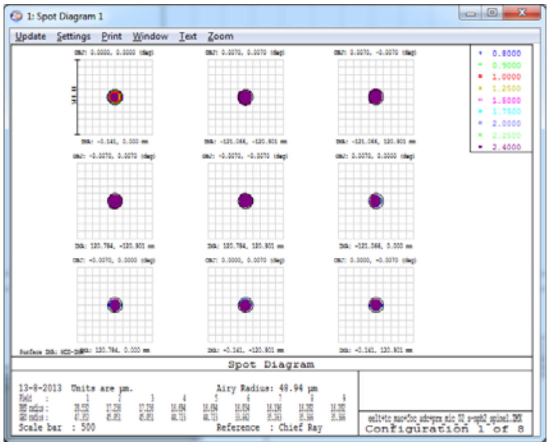

```
13-8-2013  Units are µm.                 Airy Radius: 48.94 µm
Scale bar  : 500                         Reference  : Chief Ray
Configuration 1 of 8
```

Figure 15 Spot diagrams for zenith in the MICADO detector plane. Scale is 500 microns.

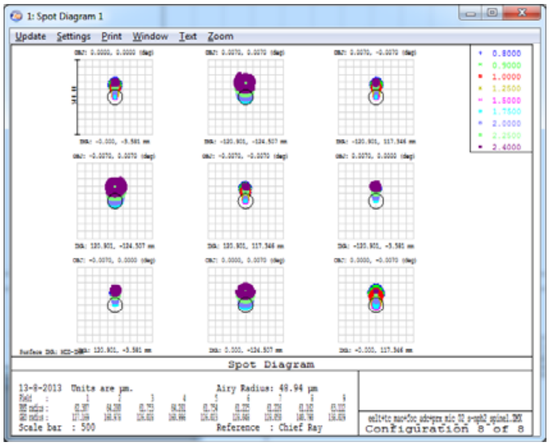

```
13-8-2013  Units are µm.                 Airy Radius: 48.94 µm
Scale bar  : 500                         Reference  : Chief Ray
Configuration 8 of 8
```

Figure 16 Spot diagrams for zenith angle 65 degrees. Scale is 500 microns.

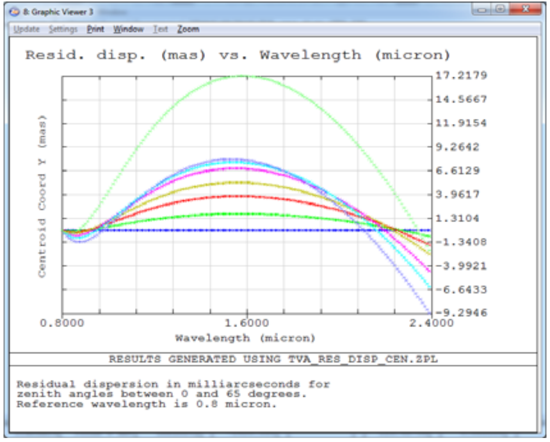

```
RESULTS GENERATED USING TVA_RES_DISP_CEN.ZPL

Residual dispersion in milliarcseconds for
zenith angles between 0 and 65 degrees.
Reference wavelength is 0.8 micron.
```

Figure 17 Residual dispersion in mas (PV is 27 mas) for the zenith angles 0, 15, 30, 40, 50, 55, 60 and 65 degrees.

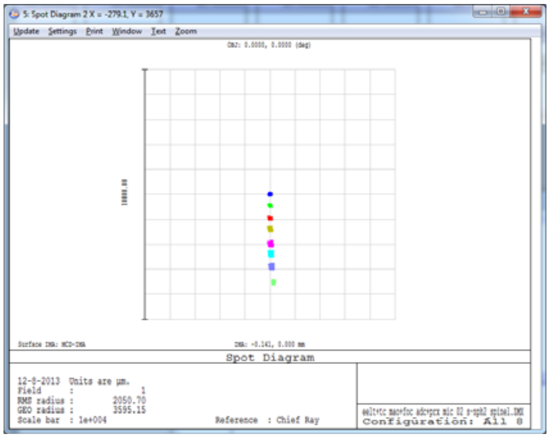

```
12-8-2013  Units are µm.
Field       :           1
RMS radius  :     2050.70
GEO radius  :     3595.15
Scale bar   : 1e+004                     Reference  : Chief Ray
Configuration: All 8
```

Figure 18 Spot drift is around 7mm as the ADC rotates. Spots for zenith angles 0, 15, 30, 40, 50, 55, 60 and 65 degrees are shown.

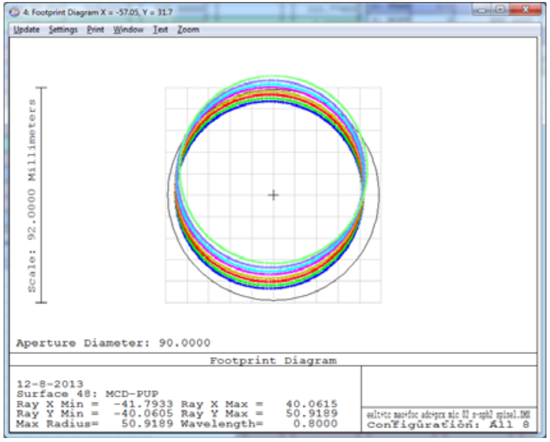

```
Aperture Diameter: 90.0000

12-8-2013
Surface 48: MCD-PUP
Ray X Min =  -41.7933 Ray X Max =   40.0615
Ray Y Min =  -40.0605 Ray Y Max =   50.9189
Max Radius=   50.9189 Wavelength=    0.8000
Configuration: All 8
```

Figure 19 Pupil shear for 0.8 micron wavelength. The colors represent different zenith angles.

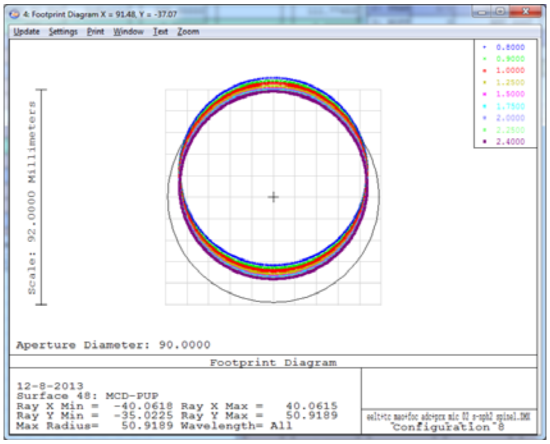

```
Aperture Diameter: 90.0000

12-8-2013
Surface 48: MCD-PUP
Ray X Min =  -40.0618 Ray X Max =   40.0615
Ray Y Min =  -35.0225 Ray Y Max =   50.9189
Max Radius=   50.9189 Wavelength= All
Configuration 8
```

Figure 20 Pupil shear for 65 degrees zenith angle. The colors represent wavelengths between 0.8-2.4 micron.

4.2.3 Zero deviation counter rotation based ADC (based on S-NPH2 and Spinel)

In the following the ADC configuration from section 2.2. was re-optimized in order to reduce the spot drift (the result can be seen in Figure 22). The spot diagrams are almost identical to the previous design so they are not shown below.

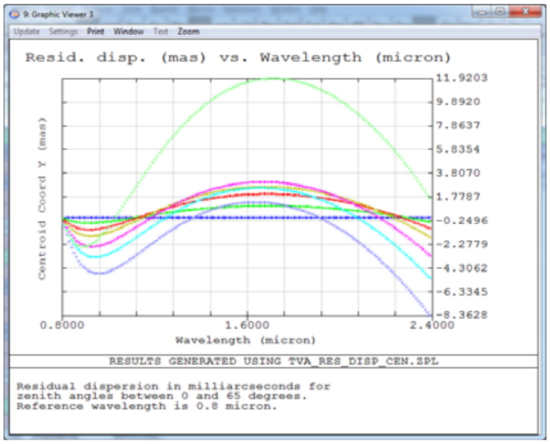

```
RESULTS GENERATED USING TVA_RES_DISP_CEN.ZPL

Residual dispersion in milliarcseconds for
zenith angles between 0 and 65 degrees.
Reference wavelength is 0.8 micron.
```

Figure 21 Residual dispersion in mas (PV is 20 mas) for the zenith angles 0, 15, 30, 40, 50, 55, 60 and 65 degrees.

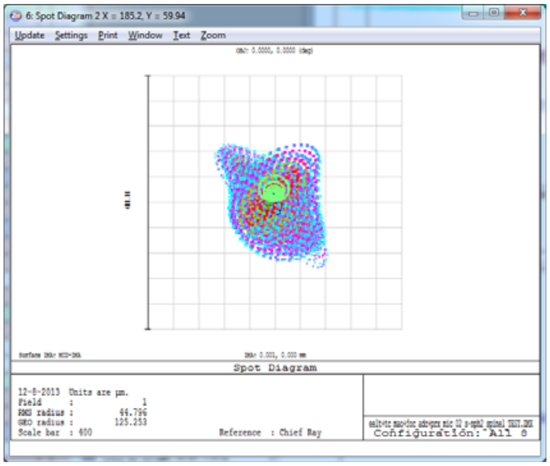

```
12-8-2013  Units are µm.
Field     :           1
RMS radius :       44.796
GEO radius :      125.253
Scale bar  : 400                 Reference  : Chief Ray
                                        Configuration: All 8
```

Figure 22 Spot drift is reduced to essentially 0 as the ADC rotates.

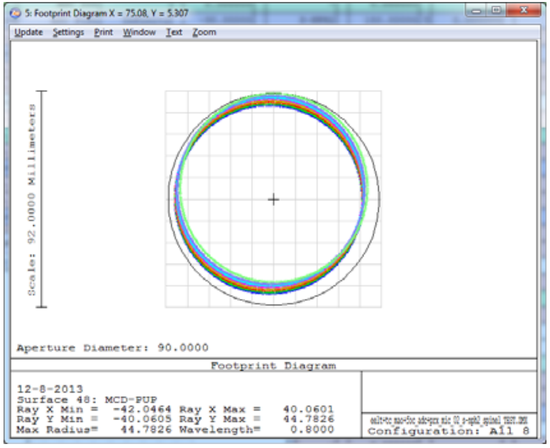

```
12-8-2013
Surface 48: MCD-PUP
Ray X Min =   -42.0464 Ray X Max =    40.0601
Ray Y Min =   -40.0605 Ray Y Max =    44.7826
Max Radius=    44.7826 Wavelength=     0.8000
                                        Configuration: All 8
```

Figure 23 Pupil shear for different wavelength is also reduced (here the 0.8 micron pupils can be seen). The colors represent different zenith angles.

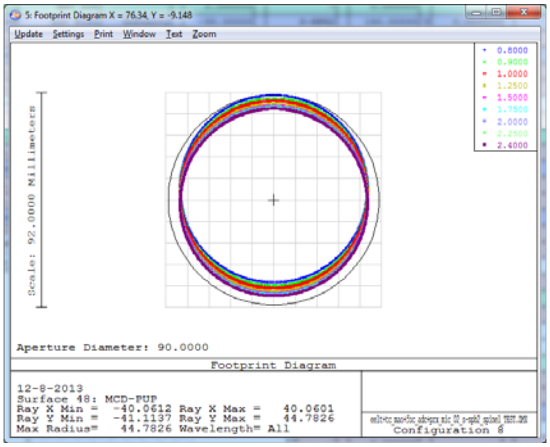

```
12-8-2013
Surface 48: MCD-PUP
Ray X Min =   -40.0612 Ray X Max =    40.0601
Ray Y Min =   -41.1137 Ray Y Max =    44.7826
Max Radius=    44.7826 Wavelength= All
                                        Configuration 8
```

Figure 24 Pupil shear for 65 degrees zenith angle. The colors represent wavelengths between 0.8-2.4 micron.

4.2.4 Linear ADC

In the following the linear ADC (with two ZnSe prisms) is investigated. The layouts for 0 and 65 degree zenith angle scenario are shown below. The travel of the second component is 300mm in this particular case, but it can be reduced to 150mm if need without introducing significant optical aberrations (the prism top angle increase as the maximum travel shortens between the components). As one of the ZnSe prisms is moving, the optical axis is displaced and also some defocus is introduced. The optical axis decentre is 40mm directly after the ADC, which means 60mm spot drift in the MICADO detector plane. The defocus needed is 2.5mm for the 0-65 degree zenith angle range directly after the ADC.

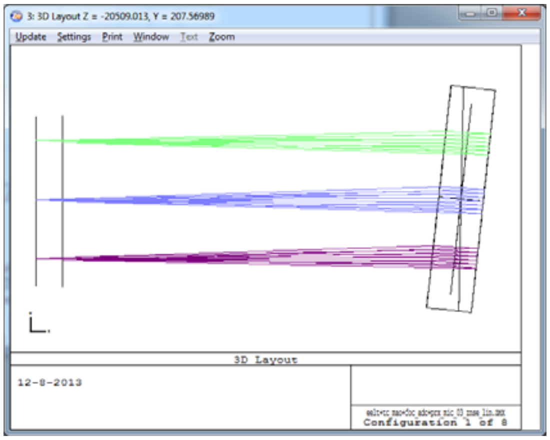

Figure 25 Layout of the linear ADC for zenith angle 0 deg.

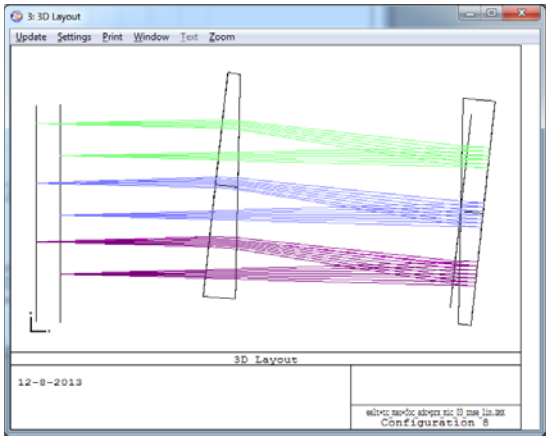

Figure 26 Layout of the linear ADC for zenith angle 65 deg.

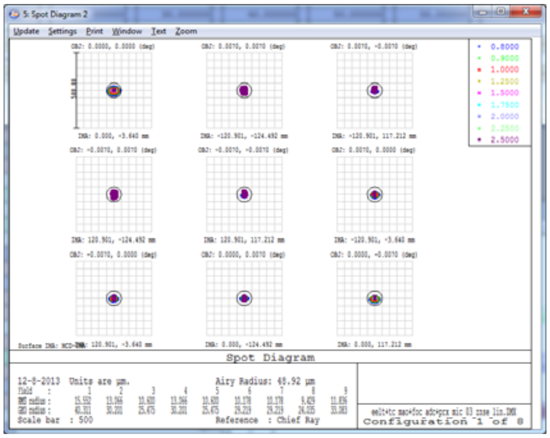

Spot Diagram
12-8-2013 Units are µm. Airy Radius: 48.92 µm
Scale bar : 500 Reference : Chief Ray
Configuration 1 of 8

Figure 27 Spot diagrams for zenith angle 0 deg in the MICADO detector plane. Scale is 500 microns.

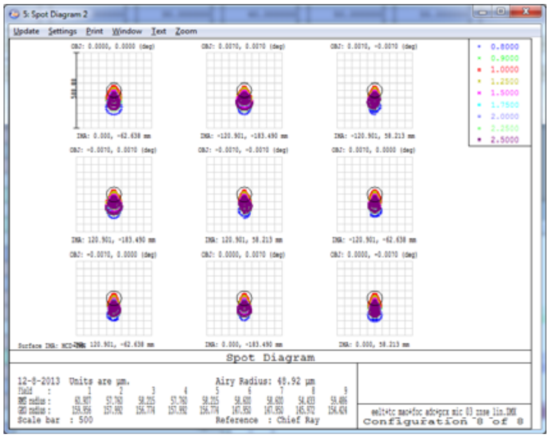

Spot Diagram
12-8-2013 Units are µm. Airy Radius: 48.92 µm
Scale bar : 500 Reference : Chief Ray
Configuration 8 of 8

Figure 28 Spot diagrams for zenith angle 65 deg. Scale is 500 microns.

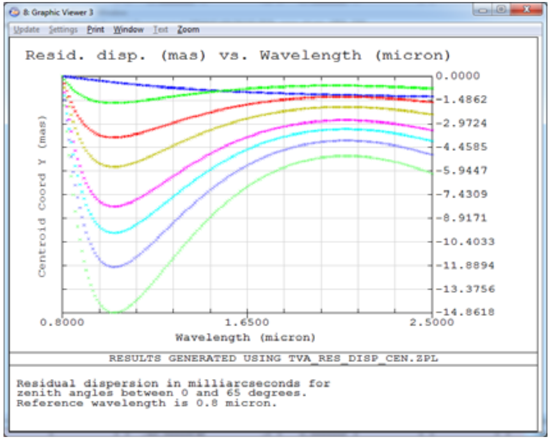

RESULTS GENERATED USING TVA_RES_DISP_CEN.ZPL

```
Residual dispersion in milliarcseconds for
zenith angles between 0 and 65 degrees.
Reference wavelength is 0.8 micron.
```

Figure 29 Residual dispersion in mas (PV is 15 mas) for the zenith angles 0, 15, 30, 40, 50, 55, 60 and 65 degrees.

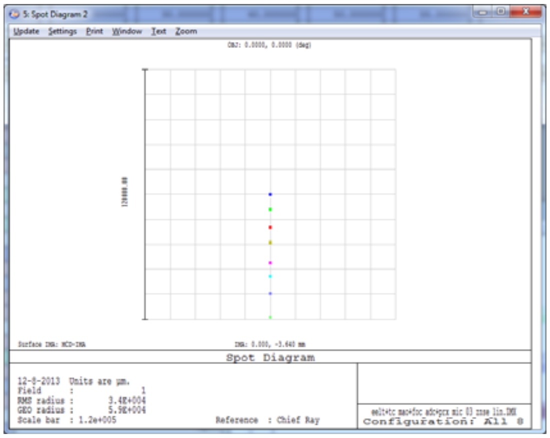

```
Spot Diagram
12-8-2013  Units are µm.
Field        :          1
RMS radius :      3.4E+004
GEO radius :      5.9E+004
Scale bar  : 1.2e+005          Reference  : Chief Ray
Configuration: All 8
```

Figure 30 Spot drift is around 60mm (!) as the ADC rotates. Spots for zenith angles 0, 15, 30, 40, 50, 55, 60 and 65 degrees are shown.

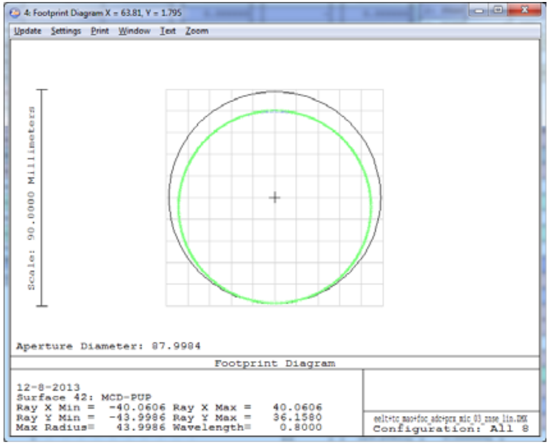

```
Aperture Diameter: 87.9984
Footprint Diagram
12-8-2013
Surface 42: MCD-PUP
Ray X Min =  -40.0606 Ray X Max =   40.0606
Ray Y Min =  -43.9986 Ray Y Max =   36.1580
Max Radius=   43.9986 Wavelength=   0.8000
Configuration: All 8
```

Figure 31 Pupil shear for 0.8 micron wavelength. The colors represent different zenith angles.

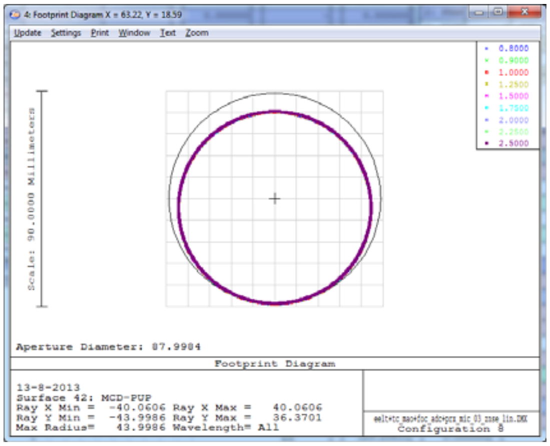

```
Aperture Diameter: 87.9984
Footprint Diagram
13-8-2013
Surface 42: MCD-PUP
Ray X Min =  -40.0606 Ray X Max =   40.0606
Ray Y Min =  -43.9986 Ray Y Max =   36.3701
Max Radius=   43.9986 Wavelength= All
Configuration 8
```

Figure 32 Pupil shear for 65 degrees zenith angle. The colors represent wavelengths between 0.8-2.5 micron.

4.2.5 Zero deviation linear ADC

In the following the ADC configuration from section 2.4. was re-optimized in order to reduce the spot drift in the focal plane. The maximum travel between the components was increased to 400mm to reduce prism top-angles. The prism materials are ZnSe and ZnS. S-NPH2 and SPINEL were also considered as materials, but the prism top angles and thus the prism sizes became extremely large.

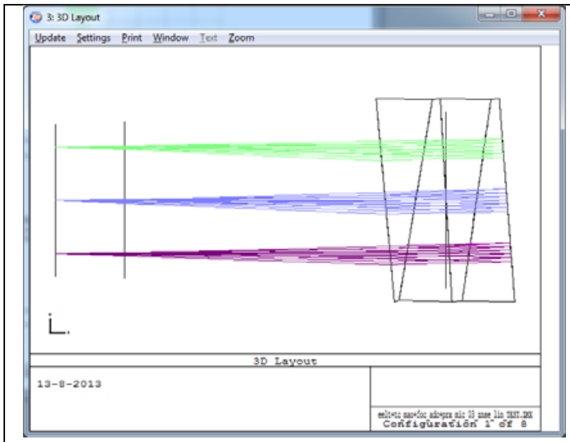

Figure 33 Layout of the linear ADC for zenith angle 0 deg.

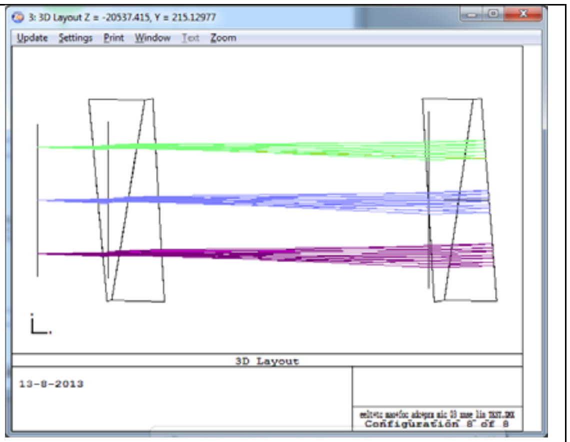

Figure 34 Layout of the linear ADC for zenith angle 65 deg.

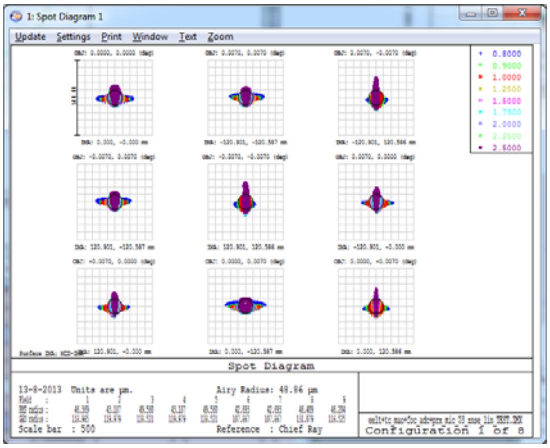

```
13-8-2013  Units are µm.               Airy Radius: 48.86 µm
Scale bar  : 500                       Reference  : Chief Ray
Configuration 1 of 8
```

Figure 35 Spot diagrams for zenith angle 0 deg in the MICADO detector plane. Scale is 500 microns.

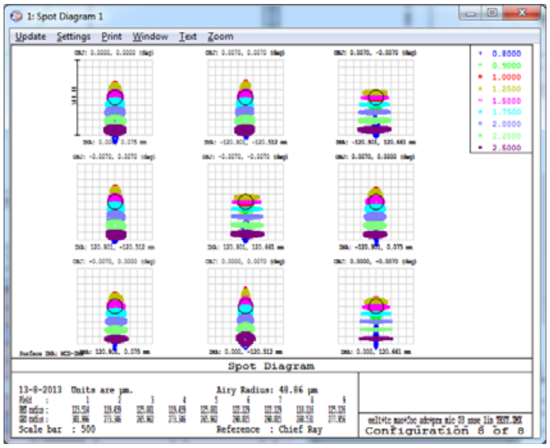

```
13-8-2013  Units are µm.               Airy Radius: 48.86 µm
Scale bar  : 500                       Reference  : Chief Ray
Configuration 8 of 8
```

Figure 36 Spot diagrams for zenith angle 65 deg. Scale is 500 microns.

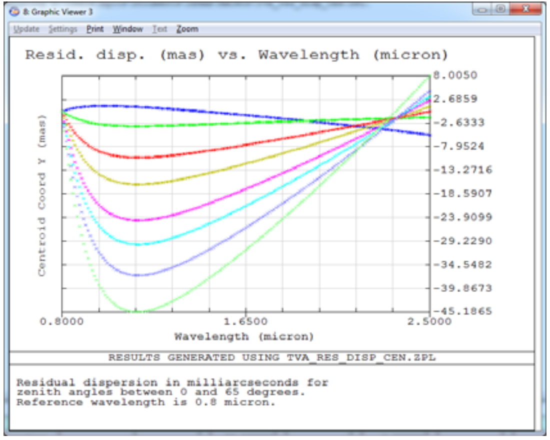

```
Residual dispersion in milliarcseconds for
zenith angles between 0 and 65 degrees.
Reference wavelength is 0.8 micron.
```

Figure 37 Residual dispersion in mas (PV is 53 mas) for the zenith angles 0, 15, 30, 40, 50, 55, 60 and 65 degrees.

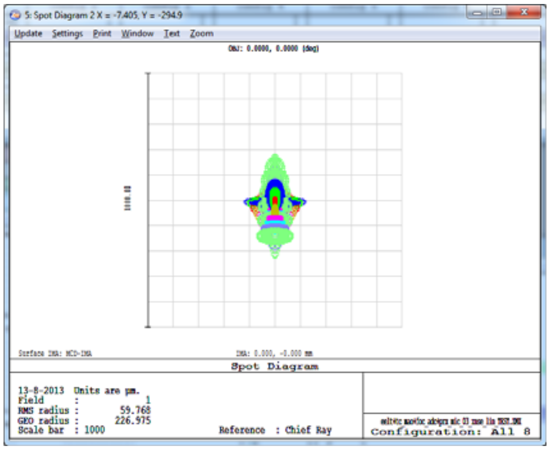

```
13-8-2013  Units are µm.
Field      :          1
RMS radius :     59.768
GEO radius :    226.975
Scale bar  : 1000                  Reference  : Chief Ray
Configuration: All 8
```

Figure 38 Spot drift is reduced completely as the ADC rotates. Spots for zenith angles 0, 15, 30, 40, 50, 55, 60 and 65 degrees are shown.

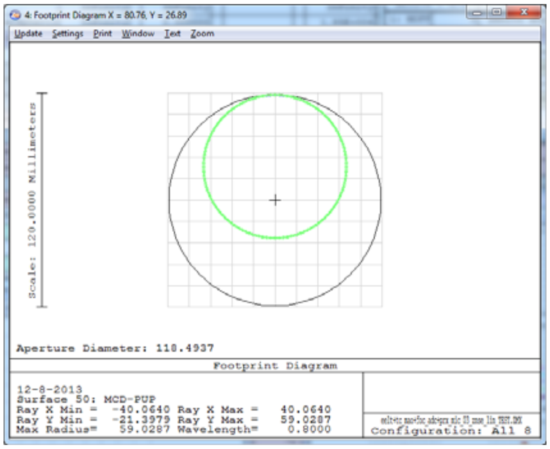

```
Aperture Diameter: 118.4937
12-8-2013
Surface 50: MCD-PUP
Ray X Min =  -40.0640 Ray X Max =   40.0640
Ray Y Min =  -21.3979 Ray Y Max =   59.0287
Max Radius=   59.0287 Wavelength=    0.8000
Configuration: All 8
```

Figure 39 Pupil shear for 0.8 micron wavelength. The colors represent different zenith angles. The optical axis is tilted after the ADC, this is shown up as global pupil decentre.

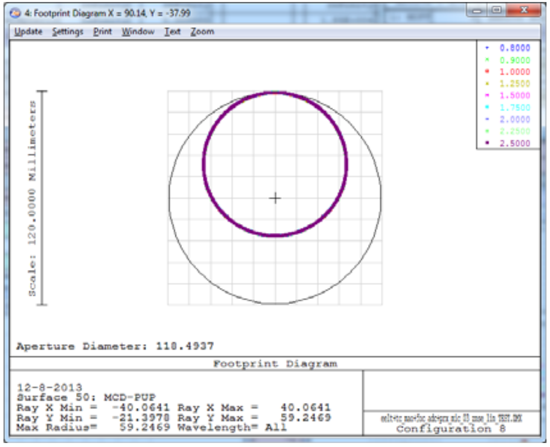

```
Aperture Diameter: 118.4937
12-8-2013
Surface 50: MCD-PUP
Ray X Min =  -40.0641 Ray X Max =   40.0641
Ray Y Min =  -21.3978 Ray Y Max =   59.2469
Max Radius=   59.2469 Wavelength= All
Configuration 8
```

Figure 40 Pupil shear for 65 degrees zenith angle. The colors represent wavelengths between 0.8-2.5 micron.

4.2.6 Linear ADC with flat mirror

In the following the linear ADC is shown, when used together a 45 degree fold mirror that can be translated. With the translation of the fold mirror the spot drift in the focal plane can be compensated and only the defocus changes for the different configurations. In the following two figures the layout is shown first without the fold mirror, then with the fold mirror (in different positions). In principle any fold mirror currently present in the system can be used for this functionality, but due to the possible footprint increase the clear aperture of certain components have to be increased.

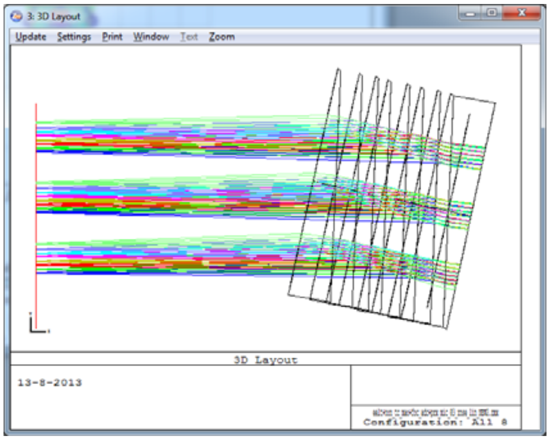

Figure 41 Layout without the fold mirror.

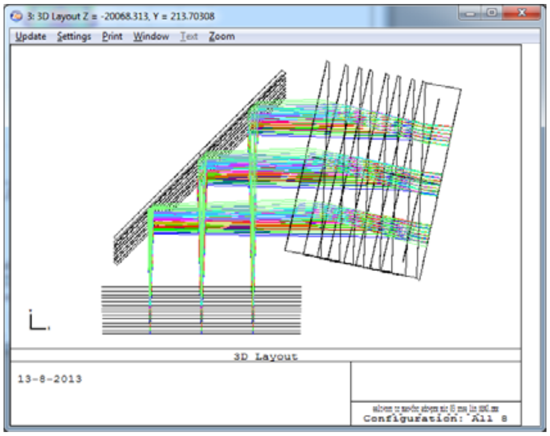

Figure 42 Layout with the fold mirror that can be translated in order to correct for the spot drift (additional defocus will be introduced).

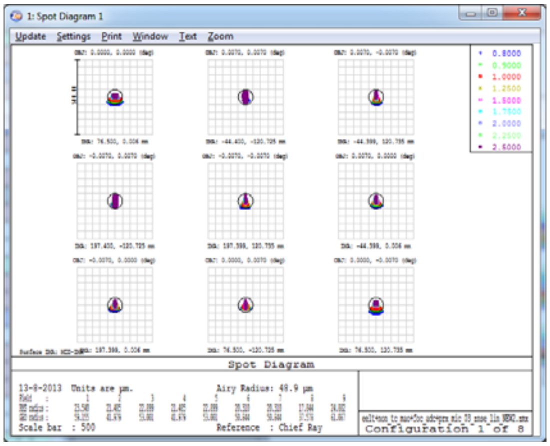

13-8-2013 Units are µm. Airy Radius: 49.9 µm
Scale bar : 500 Reference : Chief Ray

Figure 43 Spot diagrams for zenith angle 0 deg in the MICADO detector plane. Scale is 500 microns.

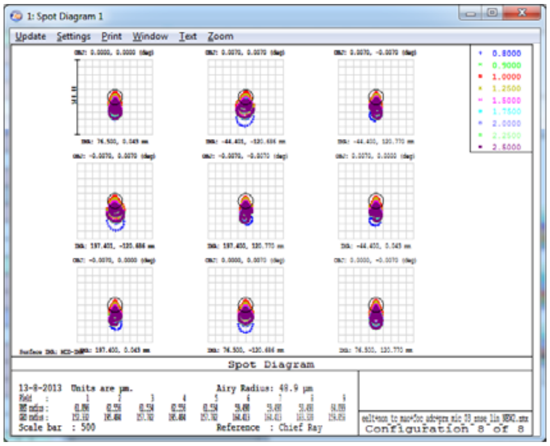

13-8-2013 Units are µm. Airy Radius: 49.9 µm
Scale bar : 500 Reference : Chief Ray

Figure 44 Spot diagrams for zenith angle 65 degrees. Scale is 500 microns.

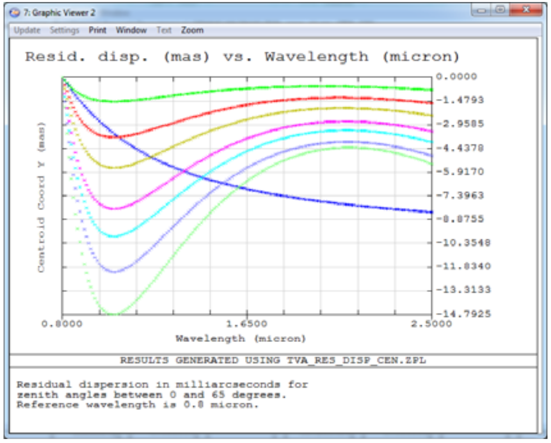

RESULTS GENERATED USING TVA_RES_DISP_CEN.ZPL

Residual dispersion in milliarcseconds for zenith angles between 0 and 65 degrees. Reference wavelength is 0.8 micron.

Figure 45 Residual dispersion in mas (PV 15 mas) for the zenith angles 0, 15, 30, 40, 50, 55, 60 and 65 degrees.

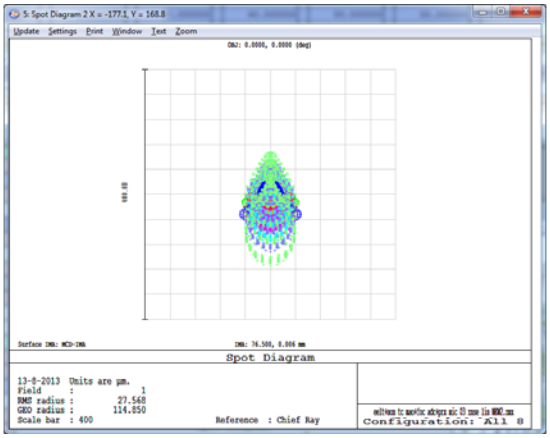

13-8-2013 Units are µm.
Field : 1
RMS radius : 27.568
GEO radius : 114.850
Scale bar : 400 Reference : Chief Ray

Figure 46 Spot drift is reduced completely as the ADC rotates.

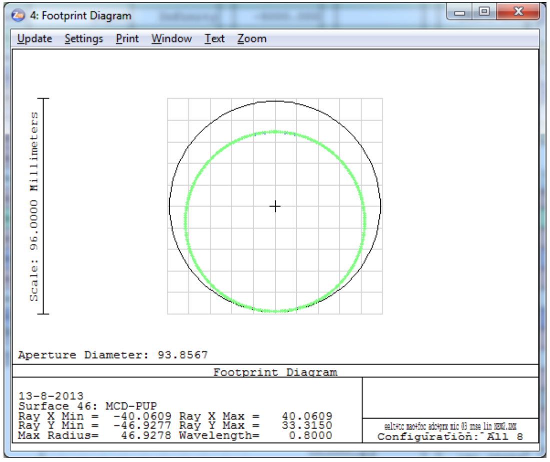

Aperture Diameter: 93.8567

13-8-2013
Surface 46: MCD-PUP
Ray X Min = -40.0609 Ray X Max = 40.0609
Ray Y Min = -46.9277 Ray Y Max = 33.3150
Max Radius= 46.9278 Wavelength= 0.8000

Figure 47 Pupil shear for 0.8 micron wavelength. The colors represent different zenith angles.

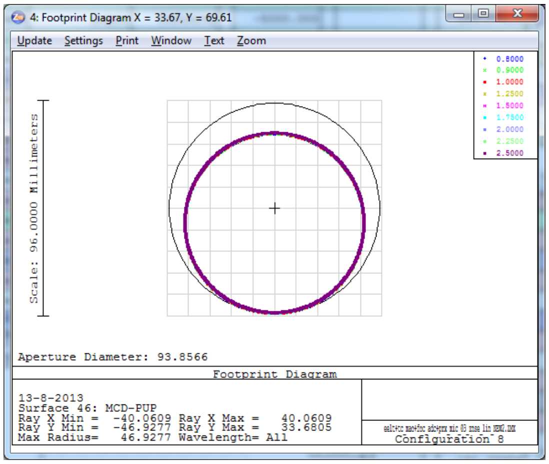

Aperture Diameter: 93.8566

13-8-2013
Surface 46: MCD-PUP
Ray X Min = -40.0609 Ray X Max = 40.0609
Ray Y Min = -46.9277 Ray Y Max = 33.6805
Max Radius= 46.9277 Wavelength= All

Figure 48 Pupil shear for 65 degrees zenith angle. The colors represent wavelengths between 0.8-2.5 micron.

4.2.7 Astrometric distortions

The astrometric distortions were determined by ray-tracing the chief ray in ZEMAX and plotted according to the description in Section 4.1.1.

	Image Plane ADC v1	Pupil Plane ADC v1	Image Plane ADC v2	Pupil Plane ADC v2	Linear ADC v1
I	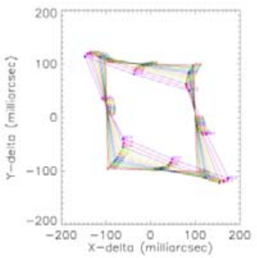	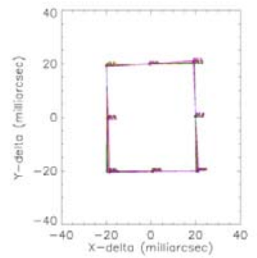	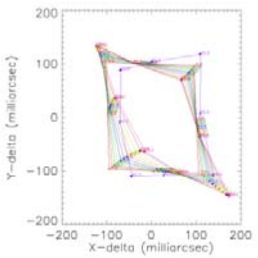	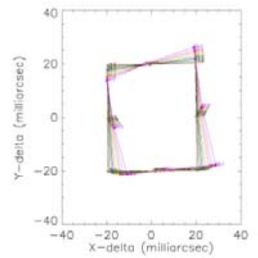	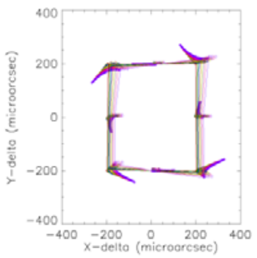
J	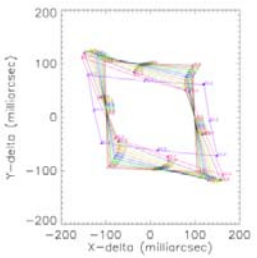	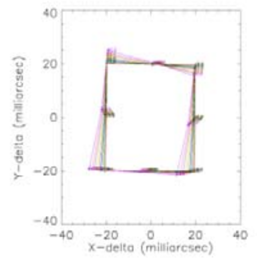	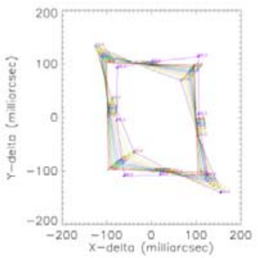	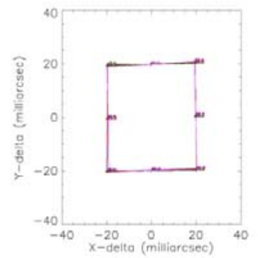	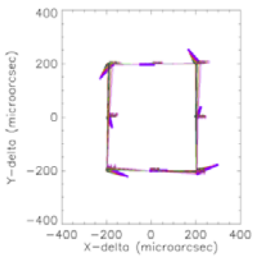
H	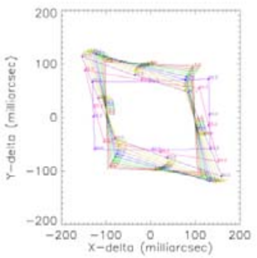	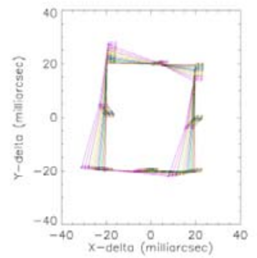	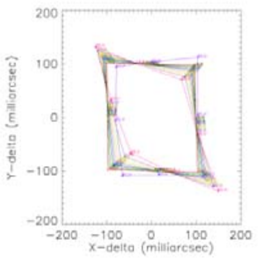	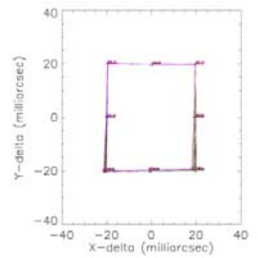	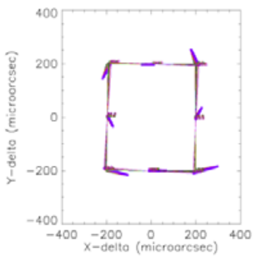
K	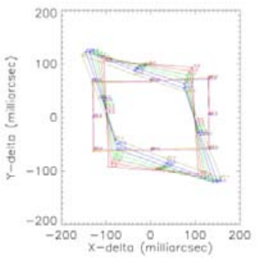	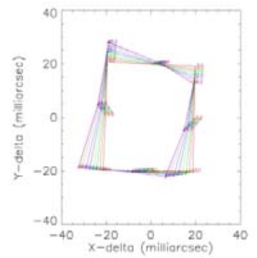	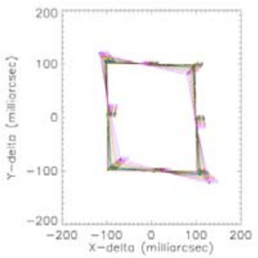	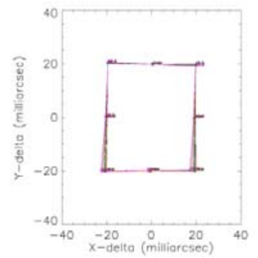	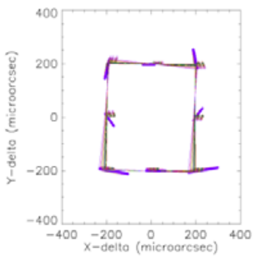
	Scale: 400 milliarcsec	*Scale: 80 milliarcsec*	*Scale: 400 milliarcsec*	*Scale: 80 milliarcsec*	*Scale: 800 microarcsec*

Figure 49. In the above 20 plots the difference in distance between image center and 8 field points at the edge of the MICADO field of view. What is shown is the relative distance variation between these points at zenith distance of 0 and given zenith distance (up to 60 degrees, given by different colors). For reference, the zero-position is given as a square. From top to bottom the different bands are shown: I, J, H and K-band. The plots, from left to right are for the first ADC study counter-rotating image plane ADC, the first ADC study counter-rotating pupil plane ADC, the current counter-rotating image plane ADC, the current counter rotating pupil plane ADC and an image plane Linear ADC. Notice the difference in scale between the various plots, as indicated with the full width of each box on the bottom row of the table. The points on the square are the renormalized field positions.

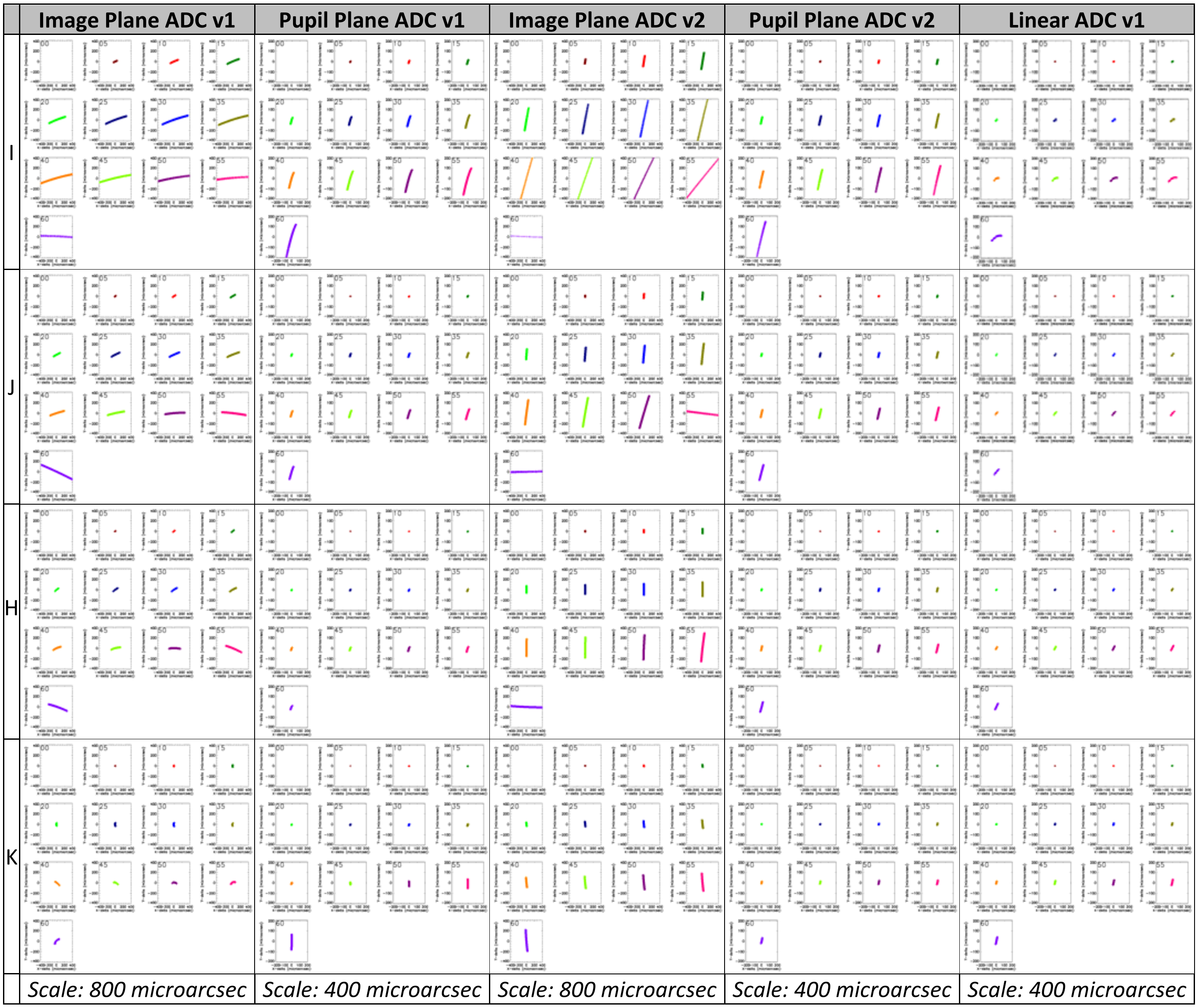

Figure 50. The layout of the 20 plots above is similar as in Figure 49: From top to bottom the different bands are shown: I, J, H and K-band. The plots, from left to right are for the first ADC study counter-rotating image plane ADC, the first ADC study counter-rotating pupil plane ADC, the current counter-rotating image plane ADC, the current counter rotating pupil plane ADC and an image plane Linear ADC. Notice the difference in scale between the various plots, as indicated by the full size of the plotted box on the bottom row of the table. In the above 8 plots the residual chromatic error is shown for one of the points at the edge of the MICADO field. The residual chromatic error is the wavelength dependent distance between center and corner point. What is shown in the 13 sub-plots is the difference between the effect a zenith distance of 0 and given zenith distance from 0 up to 60 degrees at 5 degree interval. Each point indicates the position of a different wavelength within the band, creating a line or curve.

From Figure 49 follows that from the currently investigated ADCs, the ideal linear ADC placed in the image plane performs best, followed by the counter-rotating pupil ADC. In the case of the linear

ADC, the performance is mainly limited by the residual chromatic distortions, while the pupil plane ADC still has some residual distortion, but these are largely a linear superposition of rotation and scaling, which makes calibration rather straightforward. Figure 50 shows similar residual chromatic errors for both the pupil plane ADC as well as the linear ADC, although the performance of the linear ADC is better at the shortest wavelengths. The residual errors within a band are at the level of up to ~100 micro-arcseconds, which means that for sources with unknown, but extreme colors, the astrometry might be significantly impacted, but for a standard sample of stars, these chromatic errors will not be more than a few 10-s of micro-arcsecs and can be completely removed by combining the astrometry by multi-band photometry.

4.2.8 Intermediate conclusions (focal plane ADC-s)

We investigated different ADC configurations that can be located before the focal plane of MICADO. We compared the phase A ADC, counter rotation based and linear ADC types. In the following table the characteristics of each ADC are shown.

Table 1 Comparison of the different ADC configurations. The values are color coded for better visibility.

	Phase A ADC*	Counter rot. ADC	Counter rot 0 dev. ADC	Linear ADC	Linear 0 dev. ADC	Linear ADC with flat mirror
Optical aberrations (micron) **	50	40	40	40	70	40
Residual dispersion in mas(0.8-2.5 µm)	898	27	20	15	53	15
Spot drift in the MICADO focal plane in mm	4	7	0	60	0	0
Pupil shear as a function of wavelength (%)	5	12	4	<0,1	<0,1	<0,1
Pupil shear as a function of ADC rotation (%)	0,5	6	6	<0,1	<0,1	<0,1
Space envelope (+ small, - large)	+	+	+	-	--	+/- ***
Refocus needed (mm)	<0,01	<0,03	<0,04	2,6	2,3	42,3
Residual astrometric distortions (µas)	N/A	N/A	<20000	N/A	<100	N/A
Residual chromatic astrometric errors (µas)	N/A	N/A	>800	N/A	<150	N/A

*With non-telecentric relay before MICADO.
**Worst monochromatic RMS spot radius for 65 degree zenith angle.
***Depending whether existing fold mirror can be used.

Different ADC types have different advantages and disadvantages. If generally speaking the pupil quality is of concern in MICADO, the linear ADC-s provide the best option, but then the spot drift in the focal plane have to be tackled in some way. An adjustable fold mirror can be a solution, but then the re-focusing range increases dramatically. A zero deviation linear ADC occupies a lot of space and also it introduces a significant optical axis tilt after the ADC. If the pupil quality is not that important, the counter rotation based ADC designs are more advantageous, especially the zero-deviation version.

In any case it is recommendable that a linear ADC design and a new counter rotation based ADC design are modeled the way it was done in phase A and compare the results.

The transmission of some components is not very good in some parts of the 0.8-2.5 micron spectrum, the transmission data of these materials is shown in the Annex. Also the optical performance of the ADC configurations is detailed in the Annex.

The telecentricity and non-telecentricity of the relay before MICADO does not have an effect on the ADC performance, except for the concept A ADC, which was designed for a non-telecentric pre-optics. Nevertheless the ADC has to be designed with the whole optical system known, otherwise naturally there will be an impact on performance (e.g. ADC designed for telecentric pre-optics will not perform well with non-telecentric pre-optics).

4.3 Detailed investigation of the two best ADC candidates

From the previous section the linear ADC was selected for a follow-up study. It is compared to a counter rotation based ADC located in the pupil of the SCAO system. This latter was not investigated until a very late stage because of the lack of information of the SCAO system. Finally the S-FPL51 and S-LAH71 material pair provided the best combination to mimic the atmospheric dispersion. They are also considered to be easier to manufacture than the ZnSe-ZnS and S-NPH2 and SPINEL pairs that were investigated before.

Both of the two selected ADCs performs very well regarding pupil quality in the MICADO pupil plane (better than 0.1% pupil shear) and the residual dispersion is also very good compared to other ADC designs.

4.3.1 MICADO optical model

The paraxial model of the EELT, the SCAO system and MICADO were used to study the performance of the two ADCs. At the time of the present study, there was not a tangible and unique optical design available and furthermore the performance of the ADC was ought to be separated from other optical effects of the optical path, so the paraxial model was decided to be used.

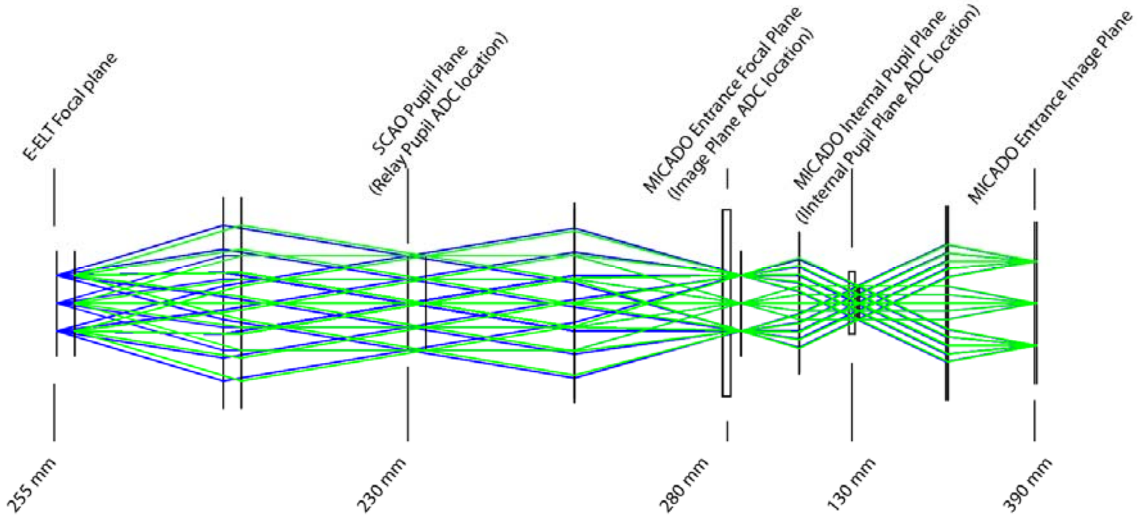

Optical diameters at given planes

4.3.2 SCAO pupil plane ADC

The SCAO pupil plane ADC is a counter rotation based ADC. S-FPL51 and S-LAH71 are the two materials that have the best possible conjoint dispersion that is able to mimic the atmospheric dispersion in the 0.72µm - 2.42µm range. The ADC consists of two identical prisms that rotate against each other. When their orientations are the same, the maximum dispersion is introduced, when they are reversed with respect to each other their dispersions null each other out. The former state corresponds to the situation, when the telescope is pointing at the maximum 60 degree zenith angle and the later, when the telescope is at zenith. In the following the layout of the ADC is shown.

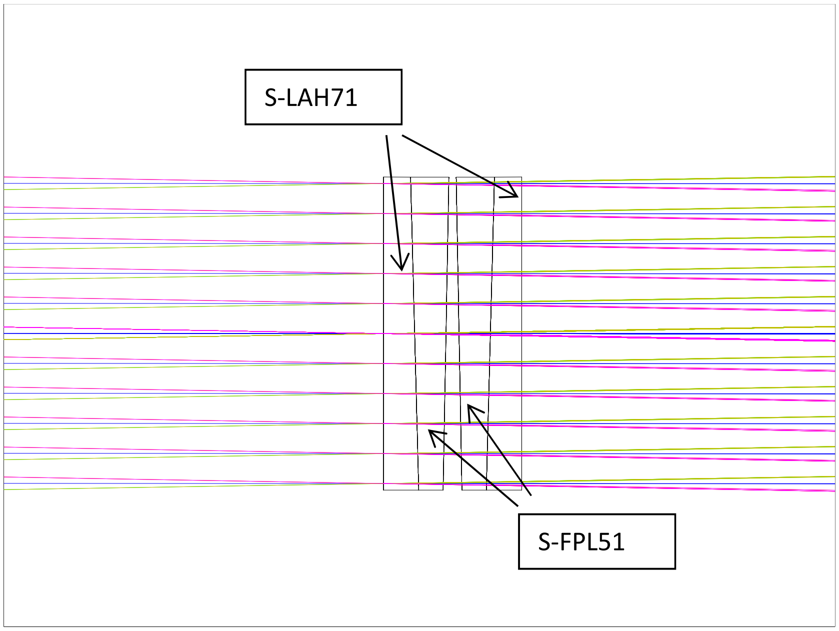

Figure 51. The layout of the SCAO pupil plane ADC. The diameter of the components is 240mm and the thickness at the vertex is 24mm.

The residual dispersion is very good, it is shown below for the total 0.72µm - 2.42µm range. Naturally this chromatic spread is much less, when only a smaller wavelength range is used.

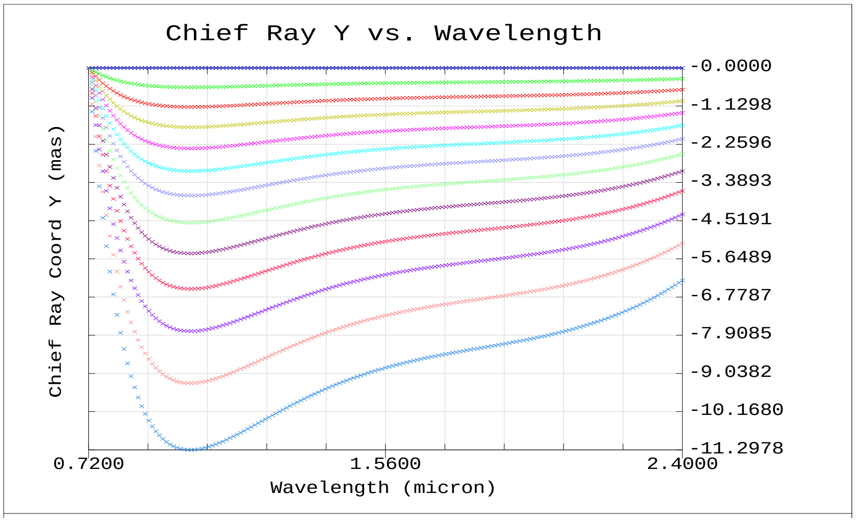

Figure 52. Residual dispersion is shown (PV 12mas). The different colors represent different zenith angles between 0 and 60 degrees.

The pupil shear was investigated inside MICADO and it was found to be almost perfect, definitely better than 0.1%. Both optical performance (residual dispersion) and MICADO pupil plane shear were evaluated at different pupil locations and it was found that they do not depend on the distance between the pupil and the location of the ADC. The transmission of the ADC materials is shown in the Annex.

4.3.3 MICADO focal plane ADC

A linear ADC in front of the MICADO focal plane is presented in the following. It consists of two identical ZnSe prisms, which form a plane parallel plate, when placed close to each other. This later scenario occurs, when the telescope is pointing at zenith; when the telescope is pointing at larger zenith angles one of the prisms is shifted away (towards the focal plane). In the design shown below the shift of the prism is 300mm. In the following the layout and the residual dispersion are shown for the linear ADC.

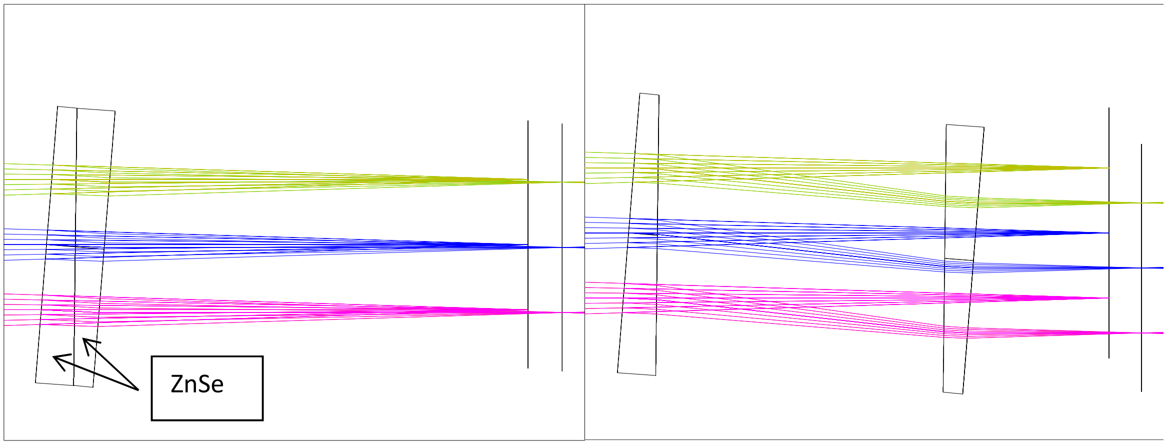

Figure 53. The linear ADC is shown, which is in the MICADO focal plane. The diameter and thickness (at the vertex) of the components are 300mm and 30mm respectively. Telescope is pointing at zenith (left), telescope is pointing at 60 degrees zenith angle (right). In the latter case the optical axis is decentered by 33.35mm.

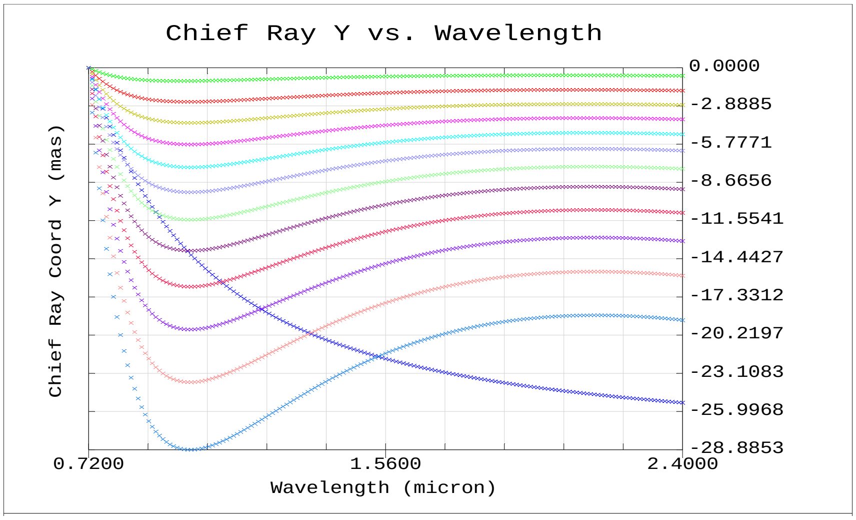

Figure 54. Residual dispersion is shown (PV 29mas). The different colors represent different zenith angles between 0 and 60 degrees.

4.3.4 Tolerances

The tolerances of the two systems were investigated and the worst offenders were identified. Using the residual dispersion as a criteria in the tolerance analysis, the tolerances on the homogeneity and the surface irregularity are the worst offenders. After the blanks are made, the re-optimization of the prism top angles is necessary knowing the material properties of the blanks.

Manufacturing tolerances investigated:

- Thickness, decentre x,y: 20 micron
- Surface tilt and component tilt:
    - 0.0048 deg (20 micron over the full diameter) for the pupil ADC
    - 0.0038 deg (20 micron over the full diameter) for the linear ADC
    - 0.0024 deg for the pupil ADC as unit
    - 0.0019 deg for the linear ADC as unit
- Index: 0.001
- Abbe: 0.1 (index and Abbe should be measured and them tits are re-optimized)
- Surface irregularity:
    - 10nm (pupil ADC)
    - 15nm (linear ADC)
- Homogeneity
    - ZnSe 4ppm
        - it means a +/-2ppm variation (H3 equivalent), with a 30mm thickness It is 30nm RMS WFE
    - S-FPL51 and S-LAH71 2ppm
        - it means a +/-1ppm variation (H2 equivalent), with a 24mm thickness It is 12nm RMS WFE
- Birefringence <=10nm/cm: this means a 24 nm RMS WFE
- Stria grade A: this means <15nm RMS WFE
- Thickness, diameter of blank: +/-0.5mm

4.3.5 ADC optical models analyzed

An overall four configurations were analyzed in detail. For each of them the adjustable parameter (counter rotation and translation of the linear ADC respectively for the two designs) was re-optimized for I, J, H and K bands.

ADC design	ADC type	Tolerances
SCAO pupil ADC	Counter rotation based	No tolerances
SCAO pupil ADC	Counter rotation based	Worst case tolerances
MICADO focal plane ADC	Linear ADC	No tolerances
MICADO focal plane ADC	Linear ADC	Worst case tolerances

A 10000 sample based Monte Carlo simulation was run using the above indicated tolerances. The tolerances followed a parabolic distribution, which yielded selected values that were more likely to be at the extreme ends of the tolerance range, rather than near the middle, as for the normal distribution. The worst samples of this Monte Carlo simulation were selected for further study presented below.

In the following the spot diagrams (also showing the nominal image quality) and the residual dispersion is shown for these worst case scenarios.

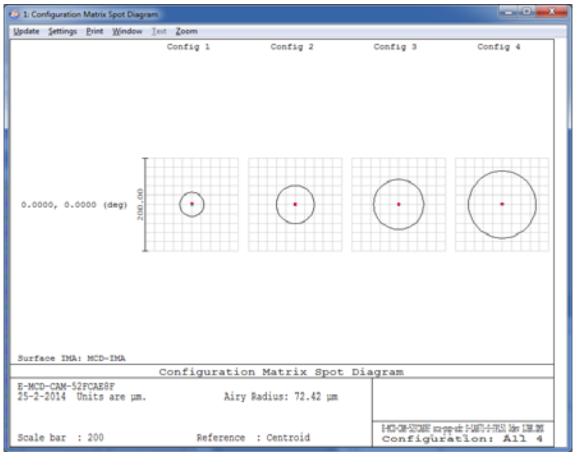

```
E-MCD-CAM-52FCAE8F
25-2-2014  Units are µm.          Airy Radius: 72.42 µm
Scale bar  : 200                  Reference  : Centroid
```

Figure 55. Spot diagrams for I, J, H and K bands for 60 degrees zenith angle for the nominal case of the pupil ADC. The Airy disk for each band is shown for the smallest wavelength.

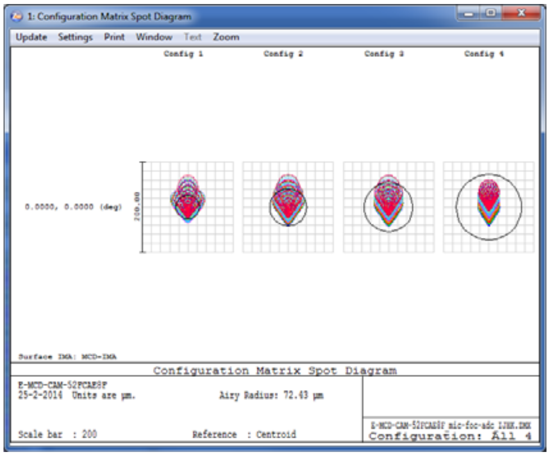

```
E-MCD-CAM-52FCAE8F
25-2-2014  Units are µm.          Airy Radius: 72.43 µm
Scale bar  : 200                  Reference  : Centroid
```

Figure 56. The same as in the previous figure but for the nominal linear ADC.

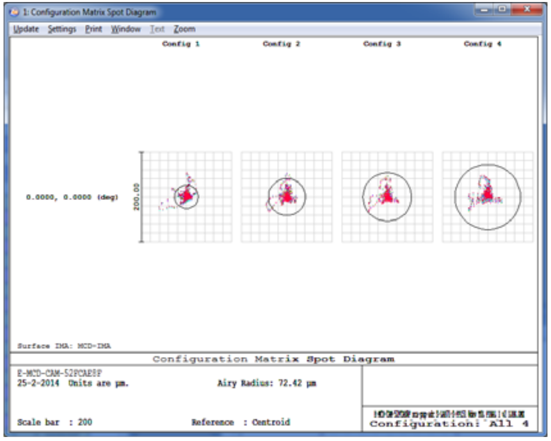

```
E-MCD-CAM-52FCAE8F
25-2-2014  Units are µm.          Airy Radius: 72.42 µm
Scale bar  : 200                  Reference  : Centroid
```

Figure 57. The same as in the previous figure but for the toleranced pupil ADC.

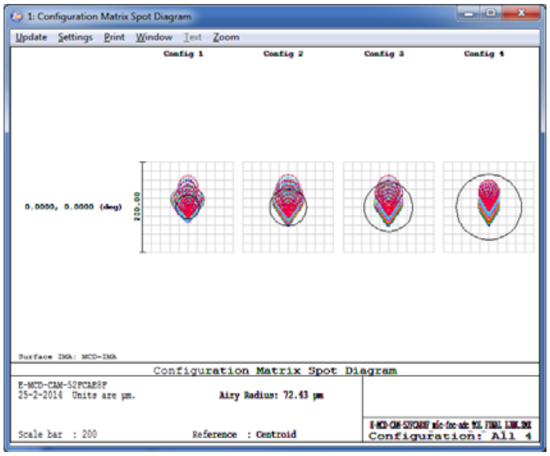

```
E-MCD-CAM-52FCAE8F
25-2-2014  Units are µm.          Airy Radius: 72.43 µm
Scale bar  : 200                  Reference  : Centroid
```

Figure 58. The same as in the previous figure but for the toleranced linear ADC.

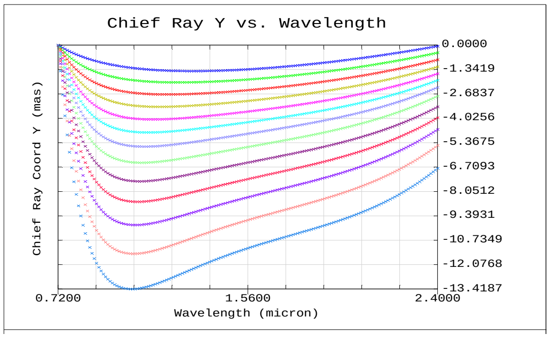

Figure 59. Residual dispersion is shown (PV 14mas) for the toleranced case of the pupil plane ADC.

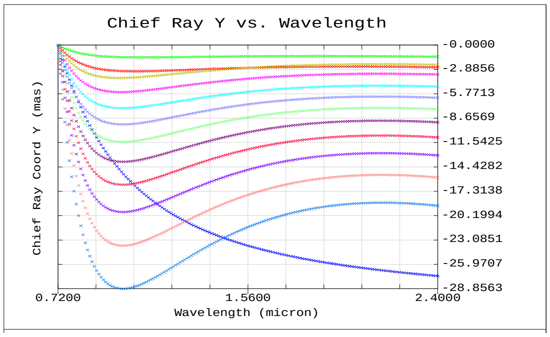

Figure 60. Residual dispersion is shown (PV 29mas) for the toleranced case of the linear ADC.

4.3.6 Astrometric distortions

The astrometric distortions were determined by ray-tracing the chief ray in ZEMAX and plotted according to the description in Section 4.1.1.

	Ideal Pupil ADC v3	Real Pupil Plane ADC 3	Ideal Linear ADC v2	Real Linear ADC v2
I	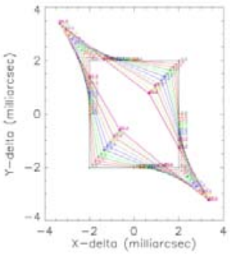	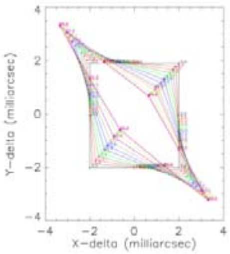	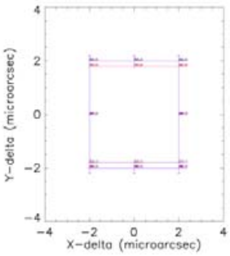	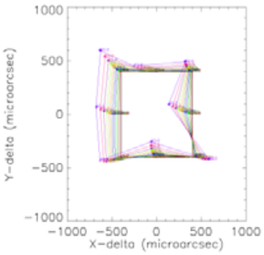
J	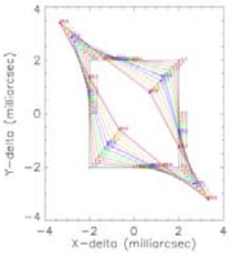	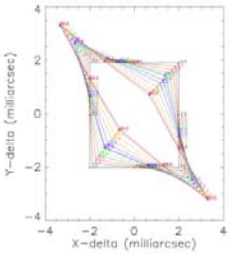	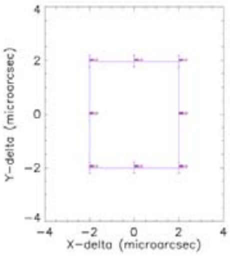	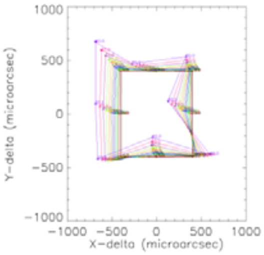
H	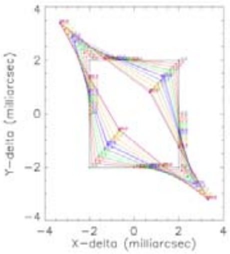	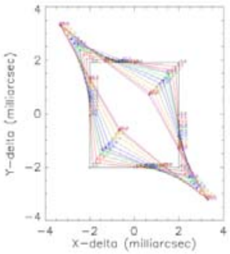	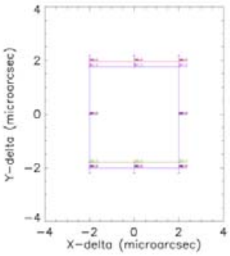	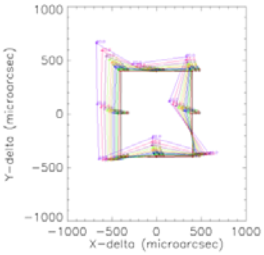
K	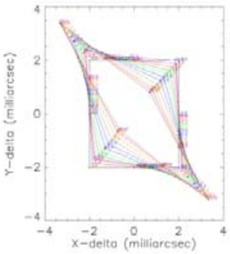	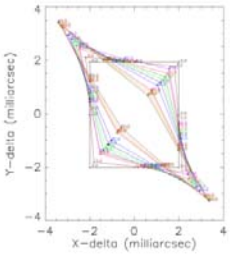	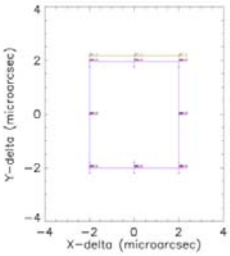	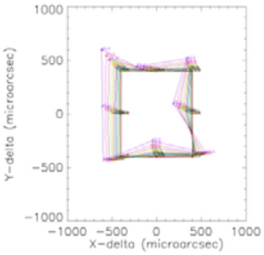
	Scale: 8 milliarcsec	*Scale: 8 milliarcsec*	*Scale: 8 microarcsec*	*Scale: 2 milliarcsec*

Figure 61. In the above 16 plots the difference in distance between image center and 8 field points on a square with sides of 10” are shown. What is shown is the relative distance variation between these points at zenith distance of 0 and given zenith distance (up to 60 degrees, given by different colors). For reference, the zero-position is given as a square. From top to bottom the different bands are shown: I, J, H and K-band The plots, from left to right are for the Ideal counter-rotating pupil plane ADC, the counter-rotating pupil plane ADC with realistic tolerances, the ideal linear ADC in the image plane and the linear ADC in the image plane with realistic tolerances. Notice that these plots only investigate the inner 10” rather than the full MICADO field of view and note the difference in scale between the various plots, as indicated with the full width of each box on the bottom row of the table. The points on the square are the renormalized field positions.

	Ideal Pupil ADC v3	Real Pupil Plane ADC 3	Ideal Linear ADC v2	Real Linear ADC v2
I	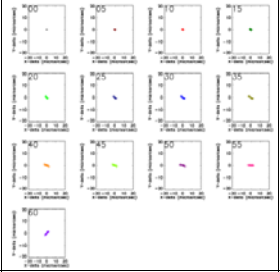	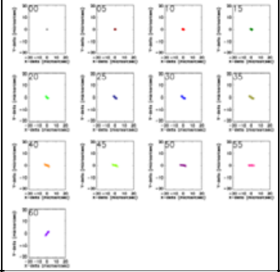	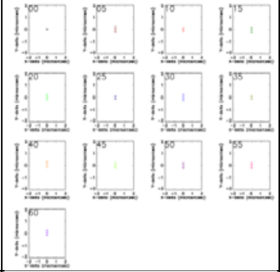	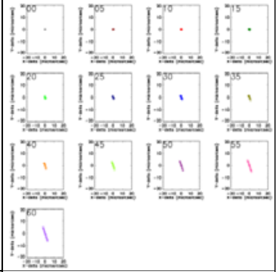
J	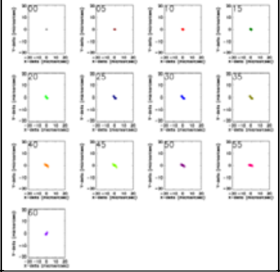	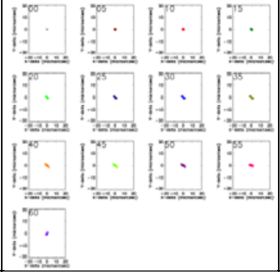	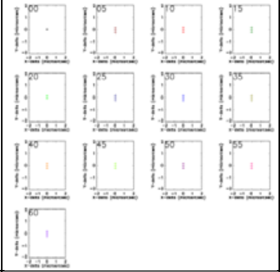	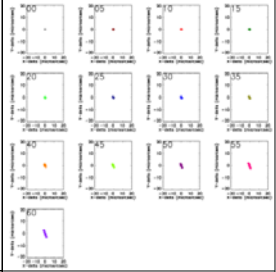
H	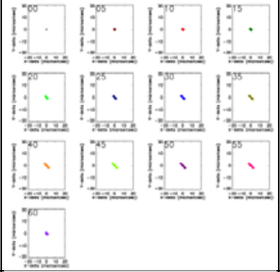	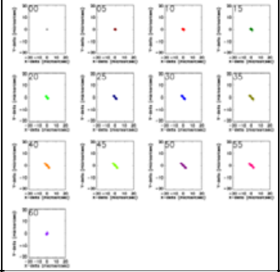	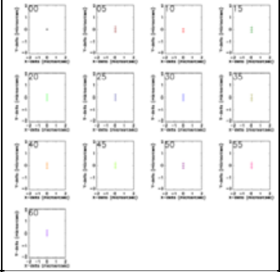	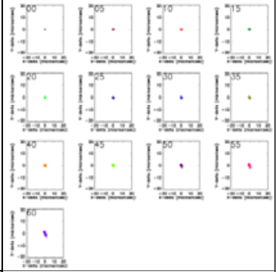
K	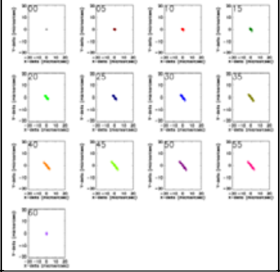	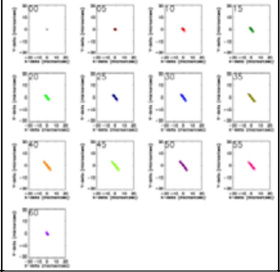	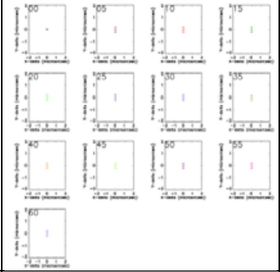	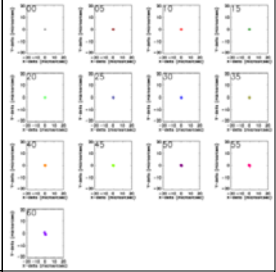
	Scale: 40 microarcsec	Scale: 40 microarcsec	Scale: 4 microarcsec	Scale: 40 microarcsec

Figure 62. The layout of the 8 plots above is similar as in Figure 61: From top to bottom the different bands are shown: I, J, H and K-band. The plots, from left to right are for the Ideal counter-rotating pupil plane ADC, the counter-rotating pupil plane ADC with realistic tolerances, the ideal linear ADC in the image plane and the linear ADC in the image plane with realistic tolerances. Notice that these plots only investigate the inner 10" rather than the full MICADO field of view and note the difference in scale between the various plots, as indicated by the full size of the plotted box on the bottom row of the table. In the above 8 plots the residual chromatic error is shown for one of the points at the edge of the MICADO field. The residual chromatic error is the wavelength dependent distance between center and corner point. What is shown in the 13 sub-plots is the difference between the effect a zenith distance of 0 and given zenith distance from 0 up to 60 degrees at 5 degree interval. Each point indicates the position of a different wavelength within the band, creating a line or curve.

Figure 61 shows the performance of the ideal ADCs versus real-world ADCs with realistic tolerances. The latter are a worst case, as explained in previous paragraphs and actual performance should be significantly better.

The first thing to notice is that the residual distortions for the counter-rotating pupil ADC seem to be very well behaved. The distortion is basically a an-isotropic linear scaling, which is very easy to calibrate with a minimal set of calibration points – this means even without a calibration mask, only a minimal number of reference stars is required to calibrate this angle-dependent distortion. Secondly, the impact of adding tolerances on the astrometric performance, as measured by the chief ray, of the pupil ADC is minimal. This ignores any decrease in performance due to decreased image quality though.

For the ideal linear ADC, there are effectively no residual distortions (all that is plotted are round-off errors by ZEMAX). When adding tolerances, there are significant residual distortions, although still at a level which is ~5x lower than for the pupil ADC. It should be noted though that the distortion pattern is highly non-linear and it will be harder to accurately describe these distortions with a small set of calibrations.

The residual chromatic astrometric errors, as shown in Figure 62 demonstrate a similar behavior. Again the astrometric performance of the pupil ADC seems to be rather insensitive to tolerances on the optical components, as where the linear ADC shows a significant increase. But in both cases, the residual errors within a band are at the level of up to ~10 micro-arcseconds, which means that for sources with unknown, but extreme colors, the astrometry might be somewhat impacted, but for a standard sample of stars, these chromatic errors will not be more than a few micro-arcseconds and can be completely removed by combining the astrometry by multi-band photometry.

Note that Figure 61 and Figure 62 cannot be directly compared to Figure 49 and Figure 50 as the latter span the full field of view of MICADO, while the plots above show only the distortions on a grid of 10” square.

4.3.7 Thermal considerations

One of the concerns that have been raised is the thermal stress introduced by variations in temperature between manufacturing and operation. Apart from survivability during transport, there are three scenarios that could be envisioned:

1. Operation at observatory standard conditions, i.e. 280K+-6.5 degrees
2. Operation at observatory stabilized conditions, i.e. 280K+-0.1 degrees
3. Operation at MICADO cooled temperatures, i.e. ~100K+-0.1 degrees

Assuming that the ADC can be integrated at observatory-standard conditions, the following table gives an overview of the relative and absolute differences in expansion between the two components of a pair of materials, based on the material properties given in Section 8.

		Pupil ADC	Linear ADC
Location	-	Pupil Plane	Image Plane
Diameter	mm	230	280
Material	-	S-LAH71/S-FPL51	ZnSe/ZnS
Thermal Expansion 1	10-6/K	13.1	7.57
Thermal Expansion 2	10-6/K	7.7	6.3
Differential expansion	µm/K	1.2	0.4
Scenario 1	µm	8.1	2.3
Scenario 2	µm	0.12	0.04
Scenario 3	µm	224	64

Table 2. Impact of expansion on combinations of materials.

Although no full FEA over the temperature ranges has been performed, there are significant the difference in expansion between two materials for the pupil plane ADC. This will most likely lead to unacceptable stresses in any solidly cemented ADC when cooled to cryogenic temperatures, and potentially in an ADC which is not temperature stabilized. Since no known index-matching fluid exists that remains its flexibility down to cryogenic temperature, this means that if the ADC needs to be cooled, the ADC needs to be constructed from independent components, adding to the complexity of the system and effectively doubling the number of surfaces of the ADC.

For the linear ADC, the difference in thermal expansion is also significant, but since the two materials are not cemented, there is no risk that this leads to manufacturing challenges.

4.4 Conclusion on ADC selection

We investigated different ADC configurations that can be located before the focal plane of MICADO and in the pupil plane of the SCAO system. We compared counter rotation based and linear ADC types.

We identified the two best ADC designs and analyzed them. It became apparent that, when looking at the nominal systems, the pupil ADC performs better, but when real tolerances are also modelled, the differences diminish between the two systems.

The manufacturing tolerances are thought to be very tight by the manufacturers and further study is recommended to find the best trade-off between the manufacturing tolerances and the performance of the system.

5 Simulations

5.1 AO Simulations and Analysis

5.1.1 AO simulations from LESIA

In order to investigate the effects of the SCAO system on we have started collaborating with Yann Clénet from LESIA, who is currently responsible for the SCAO simulations for MICADO. These simulations are stochastical simulations of the atmosphere, simulating the propagation of light through a turbulent atmosphere (with several layers), computing the required wavefront correction and applying this correction to achieve closed loop performance estimates. These simulations include:

Effect/Property	**Included**
Telescope Dimensions	38.5 m, f/17.48, secondary obscuration, spiders
Simulation Wavelength	Free to choose – phase maps at 2.2 micron provided
Guide Star Wavelength	NGS, 450-720 nm atmospheric dispersion not(?) included
Guide Star Brightness	Bright (i.e. V < 5)
Atmosphere	Standard Paranal atmosphere $r_0 = 0.129$ m Mean wind speed 14.5 m/s
Field angles	On-axis & simultaneous set of 5” + 10”
Wavefront sensor	Shack-Hartmann 77x77 sub-apertures 4x4 pixels per sub-aperture
Closed loop frequency	1 kHz
Zenith Angle	0 degrees

The following effects were NOT included:

Effect/Property	**NOT Included**
Telescope Dimensions	Segment errors Segment gaps Vibrations Pupil misalignment
Atmosphere	Atmospheric composition variations
Field angles	Simultaneous on-axis off-axis data
Closed loop frequency	Loop delays (?)
Instrument	Distortions Optical properties of the relay Non-common path errors Slowly varying wavefront errors, other than atmospheric (persistent speckles)

Simulation data are provided as residual phase maps. This allows for a full reconstruction of the PSF at any desired wavelength. In order to reduce the data volume, only 1 of every 1000 phase screens are provided, i.e. at a sampling of 1 second. For the on-axis data, we have access to 1 hour of data (~26 Gb), while for the off-axis data we have 1000 seconds (18 Gb) of parallel datasets for 5” and 10” away from the guide star.

5.1.2 Transforming simulations into images

The output images are made to match the central CCD of MICADO and has the following properties:

Property	Value
CCD Type	Hawaii-4RG 4096 x 4096 pixels 15 x 15 micron per pixel
Quantum Efficiency	CCD: 100% or supplier delivered Atmosphere: 100% or atmospheric Stellar Spectrum: 1.0 (not included)
Noise	10 ADU nominal noise, only added to provide something noisy for SEXTRACTOR NO photon noise, dark current, read noise or other noise source are currently added.
Bias	1000 ADU, , only added to provide something quasi-realistic for SEXTRACTOR
Digitization	16 bit
Stellar Brightness	Set to provide maximum 60,000 ADU on CCD
Exposure time	0.001 – 100 seconds
Pixel scale	0.003”/pixel
On-Sky CCD size	12.3” horizontal/vertical 17.2” diagonal
Stacking Procedure	Straight sum (as if single exposure!)

In order to provide images for the correct wavelength, and in later stages, to introduce distortions, the following steps are applied for each wavelength and position in the field, to transform each phase map to an image:

- The phase screen is scaled and zero-padded to provide an image with a pixel scale of 3 mas per pixel over 4096x4096 pixels.
- Sub-pixel shifts of the PSF are computed by adding a phase slope is to the phase screen. These sub-pixel shifts can include deviations depending on position and wavelength, and can be time-variable.
- The PSF is computed by a Fast Fourier Transform.
- The PSF is shifted by integer pixels to the correct location in the field (sub-pixel shifts were already applied).
- A diffraction-limited PSF is computed based on a telescope pupil with no wavefront distortion. Since this PSF is computed in the same way as the distorted PSF, it allows for a

calibration of the Strehl ratio and sanity check on the expected FWHM of the PSF as a function of wavelength.

- The PSF is normalized, either by Strehl or integrated flux and added to the sum image.
- The sum-image is normalized to reach a maximum of 60000 counts, bias and noise are added. Note

A full simulation performed this way takes approximately 5 seconds per image, per star, which already gives an indication that performing the simulation in this way is not suitable for a full simulation of a dense stellar field, nor long exposures, nor a large variation in parameter space.

5.2 Relative astrometry on simulated images

We have investigated the accuracy in relative astrometry that can be obtained on the simulated images.

We analyzed the series of single exposure images (“snapshots”) and the series of stacks of 2 time-adjacent exposures (“2-stacks”) and (similarly stacked) series of 4-stacks, 5-stacks, 10-stacks, 20-stacks, 50-stacks and 100-stacks.

We took advantage of the existing Astro-WISE infrastructure to produce and store the results, catalogs and pixel data for the set of simulations (currently approaching 1700 images and growing). Links to the data archive are given on http://wiki.astro-wise.org/projects:micado:datasets.

5.2.1 Source extraction and centroiding

The simulated exposures contain a background with a Gaussian noise of mean of 1000 ADU and sigma of 10 ADU. The two stars have peak pixel values approaching 60000 and 45000 ADU, have total fluxes of ~1E6 ADU in the central 200-300 pixels and do not contain Poisson errors. Thus their formal S/N>5500.

For a well-sampled PSF the limit to centroid measurement accuracy sigma_c_m is (e.g., Kuijken et al 2012):

- sigma_c_m ~0.7 FWHM / (S/N)

which for our simulated images translates to sigma_c_m = 1 micro-arcsec for star at 2.2 micron.

However, there could be an additional systematic error in centroiding due to:

- the speckled, not well-sampled PSF in individual snapshot which smooth out for stacked exposures (see Fig. 6.1). Due to this Sextractor detects a varying number of spurious sources in the wings of the PSFs in single snapshots. However, the central detection is dominant in terms of flux (contains at least ~5 times more flux than any other source). In sufficiently (≥10) coadded images the spurious detections are absent.
- basic centroiding: we extract sources using SExtractor measuring the position in two ways: the barycenter of the isophotal footprint and Gaussian fit to the flux distribution (i.e., X_IMAGE and XWIN_IMAGE).

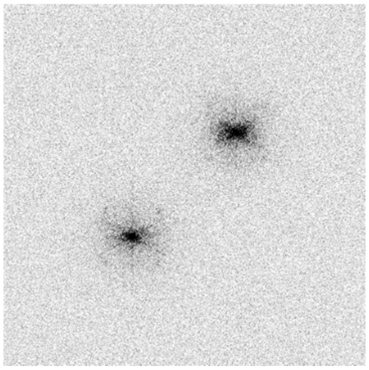

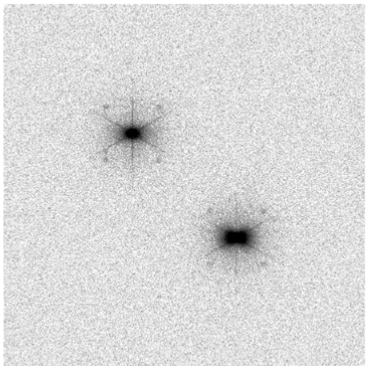

NOAO/IRAF V2.14.1 mcfarland@bolton Fri 09:45:44 21-Feb-2014
single.fits: Radial profile at 1459.89 1459.44
NOVA-SIM1

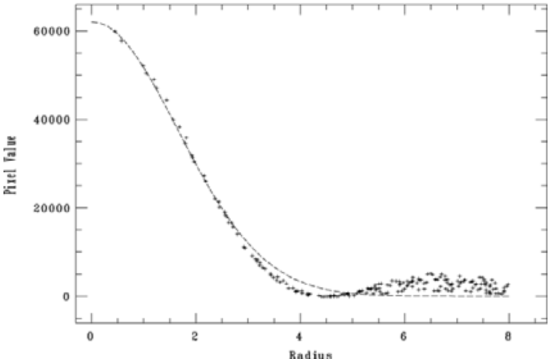

NOAO/IRAF V2.14.1 mcfarland@bolton Fri 09:53:28 21-Feb-2014
coadd100.fits: Radial profile at 1459.86 1459.72
NOVA-SIM1_Sum0100.0000

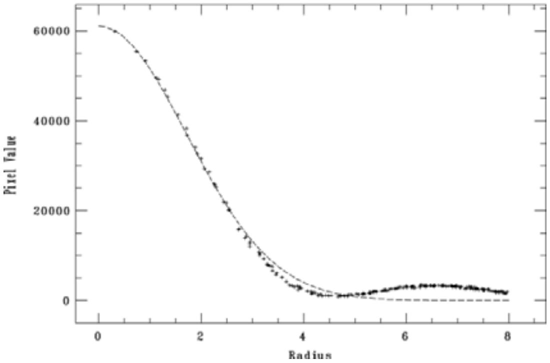

NOAO/IRAF V2.14.1 mcfarland@bolton Fri 09:48:50 21-Feb-2014
single.fits: Lines 1454-1465
NOVA-SIM1

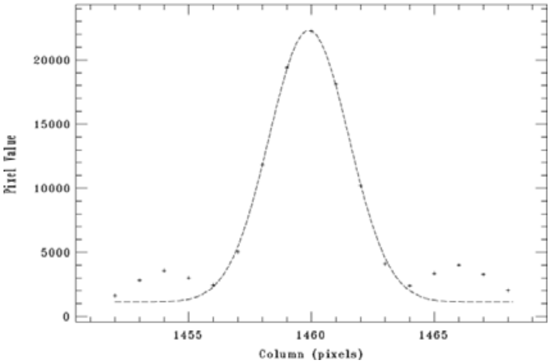

NOAO/IRAF V2.14.1 mcfarland@bolton Fri 09:53:44 21-Feb-2014
coadd100.fits: Lines 1455-1466
NOVA-SIM1_Sum0100.0000

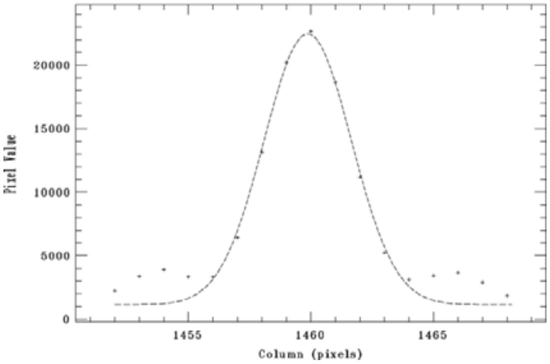

NOAO/IRAF V2.14.1 mcfarland@bolton Fri 09:49:01 21-Feb-2014
single.fits: Columns 1455-1466
NOVA-SIM1

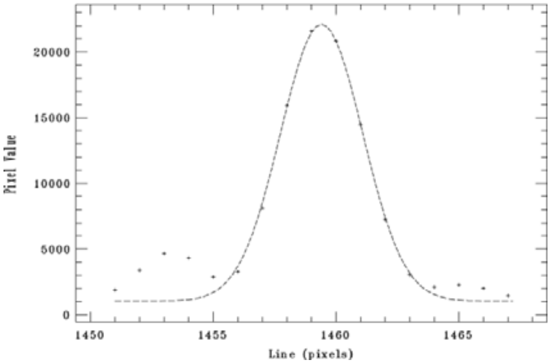

NOAO/IRAF V2.14.1 mcfarland@bolton Fri 09:53:58 21-Feb-2014
coadd100.fits: Columns 1455-1466
NOVA-SIM1_Sum0100.0000

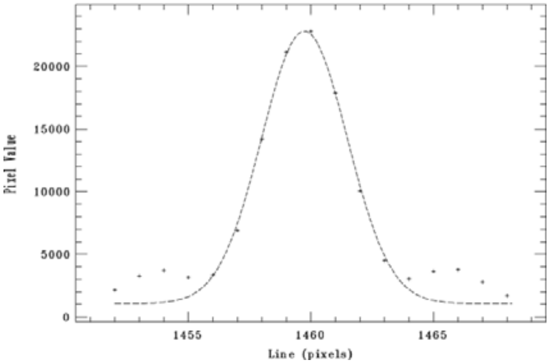

Figure 63. Images and their radial and profile plots (IRAF imexamine) of a single snapshot exposure (left) and 100 stacked snapshots (right).

We use the following information from the source extractions:

- Position measures:
  - X_IMAGE/Y_IMAGE, ERRX2_IMAGE/ERRY2_IMAGE = barycenter (flux-weighted first moment) and their error (1sigma)
  - XWIN_IMAGE/YWIN_IMAGE = Gaussian windowed measurement of these parameters
- Profile measures:
  - FWHM_IMAGE (assuming Gaussian profile)
- Flux measures:
  - FLUX_APER: flux inside a 25 pixel diameter aperture.

source ID		1	2	2-1
exposures per stack		10	10	
number of stacks		10	10	
mean number of spurious detections per stack				0.4
mean X-distance (sigma)	**[pixel]**			1178.343 (0.385)
mean XWIN-distance (sigma)	**[pixel]**			1178.379 (0.364)
mean Y-distance (sigma)	**[pixel]**			1178.539 (0.200)
mean YWIN-distance (sigma)	**[pixel]**			1178.516 (0.096)
mean X_IMAGE (sigma)	**[pixel]**	1459.876 (0.194)	2638.218 (0.361)	
mean XWIN_IMAGE (sigma)	**[pixel]**	1459.869 (0.177)	2638.248 (0.294)	
mean Y_IMAGE (sigma)	**[pixel]**	1459.752 (0.102)	2638.290 (0.133)	
mean YWIN_IMAGE (sigma)	**[pixel]**	1459.739 (0.079)	2638.255 (0.097)	
mean FWHM_IMAGE (sigma)	**[pixel]**	3.980 (0.073)	4.147 (0.085)	
mean FLUX_APER (sigma)	**[ADU]**	1485786 (62257)	1191883 (42554)	
NPIX		259	278	

Table 3. Basic information on source extraction and source distances for the 2 sources in the simulated images. Source 1 is 5arcsec away from the AO star in the X direction and source 2 is 10 arcseconds away. Both sources have same Y position as the AO star. Information is shown based on the 10 stacks that each contains 10 snapshot exposures. This table lists the information for the simulated images without ADC. The parameters are defined in the text.

Zenith Distance	[deg]	0			30			35			60		
source ID		1	2	2-1	1	2	2-1	1	2	2-1	1	2	2-1
exposures per stack		10	10		10	10		10	10		10	10	
number of stacks		10	10		10	10		10	10		10	10	
mean number of spurious detections per stack				0			0			0			0
mean X-distance (sigma)	[pixel]			1666.572 (0.442)			1666.569 (0.441)			1666.567 (0.442)			1666.570 (0.441)
mean XWIN-distance (sigma)	[pixel]			1666.536 (0.364)			1666.535 (0.364)			1666.535 (0.363)			1666.534 (0.363)
mean Y-distance (sigma)	[pixel]			-0.036 (0.121)			-0.727 (0.124)			0.229 (0.126)			0.003 (0.128)
mean YWIN-distance (sigma)	[pixel]			0.004 (0.096)			-0.685 (0.097)			0.269 (0.096)			0.042 (0.097)
mean X_IMAGE (sigma)	[pixel]	2049.086 (0.185)	3715.658 (0.383)		2049.101 (0.187)	3715.670 (0.383)		2049.097 (0.188)	3715.664 (0.383)		2049.111 (0.187)	3715.681 (0.382)	
mean XWIN_IMAGE (sigma)	[pixel]	2049.124 (0.176)	3715.659 (0.294)		2049.139 (0.176)	3715.674 (0.294)		2049.134 (0.176)	3715.670 (0.294)		2049.149 (0.176)	3715.683 (0.294)	
mean Y_IMAGE (sigma)	[pixel]	2049.029 (0.101)	2048.992 (0.097)		2037.767 (0.102)	2037.040 (0.097)		2039.741 (0.103)	2039.970 (0.098)		2021.267 (0.106)	2021.270 (0.096)	
mean YWIN_IMAGE (sigma)	[pixel]	2048.995 (0.079)	2048.999 (0.097)		2037.733 (0.079)	2037.049 (0.097)		2039.707 (0.079)	2039.976 (0.097)		2021.235 (0.079)	2021.277 (0.097)	
mean FWHM_IMAGE (sigma)	[pixel]	3.941 (0.061)	4.146 (0.054)		3.933 (0.068)	4.145 (0.056)		3.934 (0.067)	4.141 (0.057)		3.930 (0.056)	4.122 (0.063)	
mean FLUX_APER (sigma)	[ADU]	1472070 (49882)	1180005 (38939)		1490360 (52927)	1194461 (41288)		1493535 (53225)	1197191 (41426)		1487282 (50494)	1192211 (39429)	
NPIX		290	301		289	303		290	303		289	302	

Table 4. Basic information on source extraction and source distances for the 2 sources in the simulated images. Source 1 is 5arcsec away from the AO star in the X direction and source 2 is 10 arcseconds away. Both sources have same Y position as the AO star. Information is shown based on the 10 stacks that each contains 10 snapshot exposures. This table give the information for the pupil plane ADC. The parameters are defined in the text.

The barycentric centroiding and Gaussian fit yielded similar results. X and Y positions typically agreed within 0.05 pixels. Distance measurements with the Gaussian fit had a slightly lower scatter (see Table 3 and Table 4). In any further analysis we therefore discuss only the Gaussian fit results.

5.2.2 Results

In all images the sources have a FWHM ~ 4 pix (12 mas), i.e., close to the diffraction limited of 13 mas at 2.2 micron. The fact that it is slightly smaller could be due to the fact that the extraction does not identify the full wings of the profile as part of a single source.

The difference in peak values (60000 ADU for the source at 5arcsec from the AO star and 45000 ADU for the source at 10 arcseconds) is expected due to an-isoplanatism (e.g. Trippe et al.)

Table 3 and Table 4 show the distance measurements are very similar for the simulations with and without ADC. They also show that the scatter in the centroid is anisotropic: it is a factor 1.5-2 higher in the X direction compared to the Y direction. This is consistent with the anisotropy expected for tilt jitter (e.g., Trippe et al, 2010)

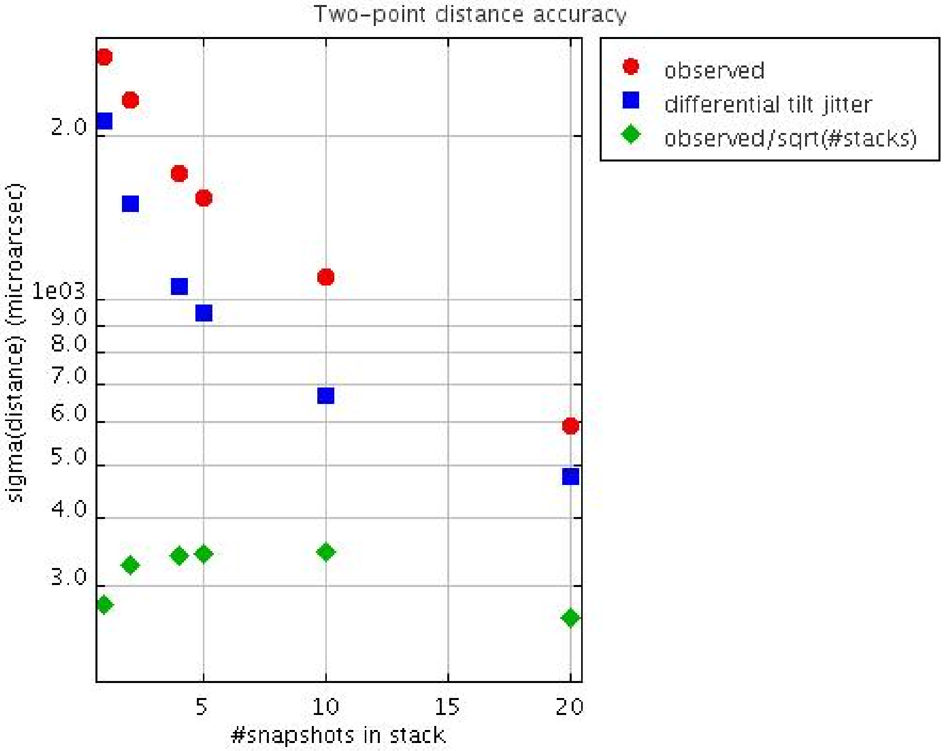

Figure 64. Standard deviation in micro-arcsecond of distance measurements measured in single snapshots and in stacks of 2,4,5, 10 and 20 exposures. The observed standard deviation of the ensemble is shown (red circles) and the standard deviation divided by SQRT(#stacks) that contain a 100 snapshots in total (green diamonds). The prediction for the effect of differential tilt jitter is also shown (blue boxes)..

We want to determine if there is a systematic floor to the accuracy with which we can determine the distance between the two stars. In Figure 64, the red circles show that the standard deviation of the distance measurements across series of different stacks (consisting of 1, 2, 4, 5, 10 and 20 exposures) scales roughly as 1/SQRT(#exposures). All stacked combinations of the 100 single exposures give a similarly accurate estimate of the distance with a standard deviation of ~300 micro-arcseconds (shown as green diamonds).

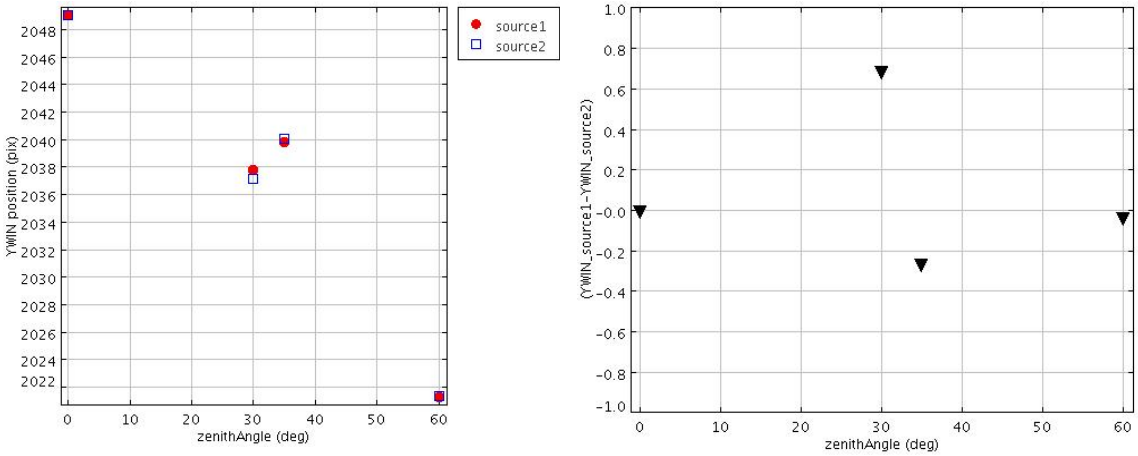

Figure 65. Position of the sources along the North-South direction (Y direction) for the simulations that include an ADC. Left: Y position as a function of zenith angle for the source at 5arcsec from AO star (red circle) and source at 10arcsec (blue square). Right: difference in the Y position of both sources as a function of zenith angle.

It is the Y position of the sources that changes for the simulations with an ADC included. Both sources have intrinsically the same Y position which measures their position in the North-South direction. Figure 65 shows that both sources show a variation in their position along North-South of up to 20 pixels moving from zenith to zenith-angles of 60deg. The relative difference in this position variation between the sources is up to a significant fraction from a pixel.

5.2.3 Discussion

We observed a 1/SQRT(#exposures) decay in scatter in relative two-point astrometry. It has diminished to an amplitude of 300 micro-arcseconds for N_{exp}=100 exposures. Such a behavior is expected for both main sources of astrometric error included in the simulations and their analysis: differential tilt jitter and random centroiding errors (Table 5). For differential tilt-jitter it is the wind crossing time on which exposures are expected to become statistically independent samplings. For centroiding errors the time scale is not known but might be on the time-scale of AO feedback loop.

Source of astrometric error	**Comments**
Differential tilt jitter σ_{TJ}	$\sigma_{TJ} \sim \theta * D^{-7/6} * (\tau/t)^{1/2}$, with θ angular distance between sources, D telescope diameter, τ wind crossing time and t integration time
Centroiding errors σ_{cen}	$\sigma_{cen} \sim(\tau/t)^{1/2}$ with τ time-scale for statistically independent centroiding and t integration time

Table 5. Sources of astrometric error which are expected to be the main contributors (e.g., Trippe et al., 2010) for the discussed simulations.

The associated timescale τ at which the exposures become statistically independent is not directly constrained by current simulations. This is due to the ambiguity whether the snapshot are representative for 1s exposures or less than that. Each snapshot has an exposure time of 0.001s while the ensemble samples the atmosphere at 1s time intervals. Figure 64 shows the predicted differential tilt jitter assuming the snapshots are representative of 1s exposures. Differential tilt jitter has as time scale the wind-crossing time which is τ ~ 3s in our case. The astrometric scatter predicted from tilt jitter only constitutes ~50 - 70% of the total observed astrometric scatter. Another contribution might come from e.g., centroiding errors. In this case the relevant time-scale could be as short as few milliseconds, which is the timescale on which the feedback loop for AO operates which causes moving speckles that might affect the centroiding.

To achieve a 35 micro-arcsecond accuracy on a single baseline (i.e., distance between science object and a reference object) the simulations imply a required integration anywhere in the range from few tens of seconds to ~1.5hr. This would yield a ~25micro-arcsec final accuracy for science cases in which a single science object has many baselines with reference sources at a typical distance of ~5arcsec.

Simulations with and without ADC show very similar results except for the Y-position which measures the North-South direction. More extensive simulations are needed to determine how well the ADC residual effects can be corrected for with calibration software. From this single baseline and few zenith angles it cannot be determined if such variations are smooth and deterministic enough to be mapped by e.g., a polynomial or look-up table.

5.2.4 Conclusion

The current simulations do not find a showstopper to achieving 50micro-arcsec astrometry within a single night with MICADO. Once the MICADO design becomes more fixed it is possible to move forward from the current basic simulations to ones that take into account the full range of sources of astrometric error listed in in this and previous ADC report. That is needed to confirm that 50 micro-arcsecond astrometry is feasible in the end-to-end system of MICADO on the E-ELT

5.2.5 Next steps

Time-continuous simulations are required. This will allow disentangling effects due to centroiding errors and differential tilt jitter.

Expand simulation to include many baselines, varying in distance and orientation with respect to AO star and with respect to North. This to establish the scaling of the accuracy with baseline size and orientation. It shall also show to which extend systematic astrometric residuals due to ADC can be corrected for via calibration software.

Expand simulations to include all sources of astrometric error. Esp. instrumental geometric distortion are potentially dominant sources that need to be quantified thoroughly.

Expand few-wavelength simulations to full pass-band simulations. This will allow to include realistic spectral energy distributions.

6 Conclusions

In this study we have investigated several ADC types, both at the pupil plane as well as in the image plane. Although theoretically the linear ADC is the best from point of view of astrometry, once manufacturing tolerances are taken into account, the differences between the linear ADC in the image plane and the counter-rotating pupil plane ADC diminishes. Boundary conditions at this point give a consortium preference to put this in the SCAO pupil plane. Any ADC is required before the MICADO entrance focal plane as the most critical requirement comes from the coronagraph. The linear ADC has advantage that it will remain usable with both the SCAO as well as the MCAO system. A real-time feedback/positioning system would be required for MICADO to maintain the focus and correct for displacements (can also be combined in a folded configuration) and such a motion compensation/vibration damping system might be required anyway, depending on the stability of the platform.

Both the linear ADC as well as the pupil ADC seem to be manufacturable, although the blank sizes are close to the limit of what can be ordered 'off-the-shelf' and the manufacturing tolerances were found to be rather tight. In the case of the pupil ADC, the optical quality of the many surfaces needs to be very good in order not to deteriorate the image quality of MICADO, specifically at the shortest wavelengths (I-band). Since the pupil ADC will be located before the SCAO system, the errors can be partly corrected by the AO system. Furthermore, the limited effort on the tolerancing focused on the worst case scenarios and some effort should be spend on investigating options to relax the requirements without deteriorating the MICADO performance.

From several simulations, it was demonstrated that several items deemed critical for the astrometric performance are indeed under control and no showstopper have been found. With a SCAO system, Astrometry to a level of 50-100 micro-arcseconds, within 5 arcseconds from the guide star seems to be feasible under favorable observing conditions, although the time required to reach these accuracies could be of the order of several hours. Extension to the MCAO performance over the full field requires sufficiently accurate simulations on the MCAO, which are not expected to become available for several years to come.

Although technically feasible, the following simulations could not be performed within the time frame of the current study and the additional data is required in order to draw stronger conclusions:

- Current simulations are limited to only two simultaneous stars and a grid of multiple stars (e.g. 10 x 10 stars) would allow for a more accurate determination of required distortion corrections.
- Current AO simulations only contain 1 in every 1000 frames. A full time sequence would allow for a better investigation of correlated noise propagation. This would require analyzing different cadences of frames everywhere between single 1 ms exposures to a full hour exposure.

With this data it will be possible to simulate if the strategy to use low level distortion polynomials can result in astrometry performance at the required level.

7 References

1. R. Stuik. G. Verdoes Klein, R. Navarro, “Achieving Full Astrometric Accuracy with MICADO and Requirements for the MICADO ADC,” Issue 1.0, 04.03.2013
2. Andrew C. Phillips, Brian J. Bauman, James E. Larkin, Anna M. Moore, Cynthia N. Niehaus, David Crampton, Luc Simard**,** The Infrared Imaging Spectrograph (IRIS) for TMT: the atmospheric dispersion corrector**’,** Proc. SPIE. 7735, Ground-based and Airborne Instrumentation for Astronomy III 77355Q (July 16, 2010) doi: 10.1117/12.856475

8 Annex

8.1 Transmission of the materials used in the study

In the following the transmission of the materials used in the study are shown.

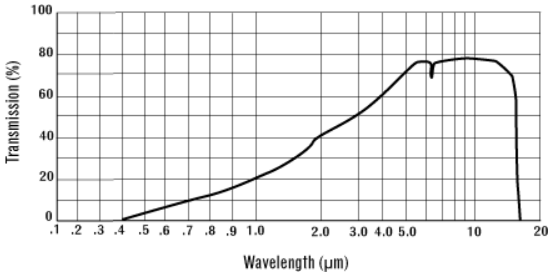

Figure 66. External transmission of ZnS (rmico.com).

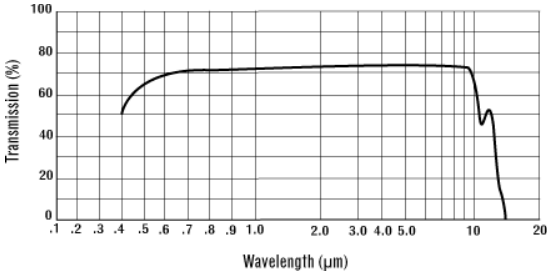

Figure 67. External transmission of ZnS/Cleartran (rmico.com).

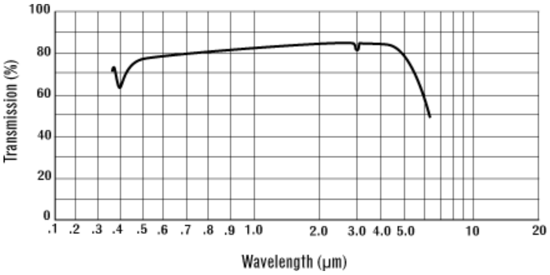

Figure 68. External transmission of Spinel ($MgAl_2O_4$) (rmico.com).

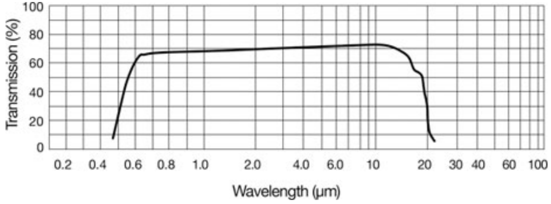

Figure 69. External transmission of ZnSe (rmico.com).

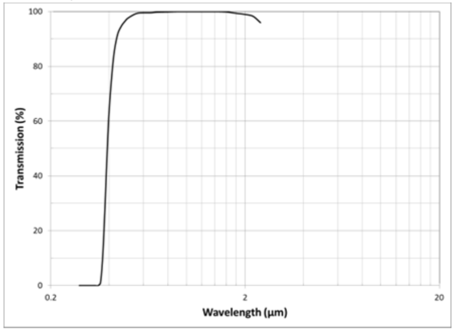

Figure 70. Internal transmission of S-LAH71 (Ohara).

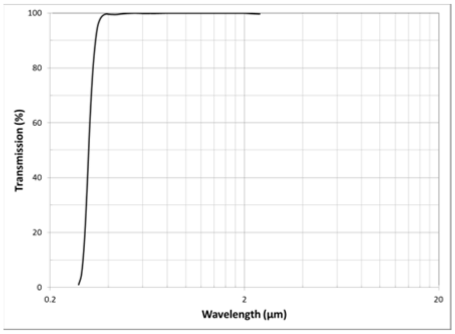

Figure 71. Internal transmission of S-FPL51 (Ohara).

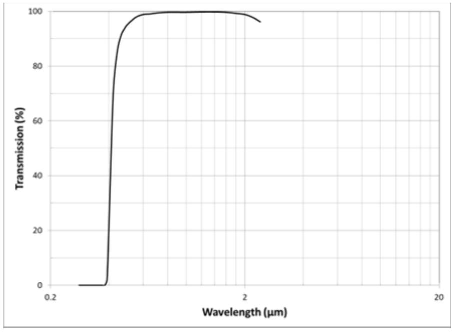

Figure 72. Internal transmission of S-NPH2 (Ohara).

8.2 Material properties of materials used in the study

	ZnSe	ZnS	S-NPH2	Spinel	S-FPL51	S-LAH71
Density (g/cm3)	5.27	4.09	3.58	3.58	3.62	4.36
Youngs Modulus GPa	67.2	74.5	99.1	276	72.7	110.0
Poisson's Ratio σ	0.29	0.28	0.249	0.26	0.299	0.281
Thermal Expansion 10^{-6}/K	7.57 (293K)	6.3 (273K)	6.7 (243-343K)	6.97 (303-473K)	13.1 (243-343K)	7.7 (243-343K)
Thermal Conductivity W/(m.K)	18	27.2	0.969	25	0.78	0.874

8.3 Optical aberrations (RMS vs field, RMS vs wave)

RMS spot radius vs. field and RMS spot radius vs. wavelength are shown for 65 degree zenith angle configuration for each ADC design.

Phase A ADC

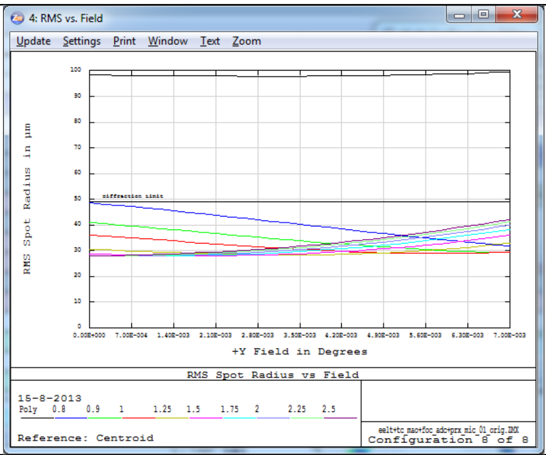

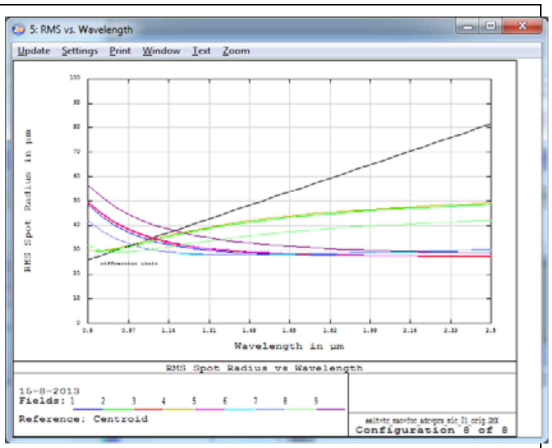

Counter rotating ADC

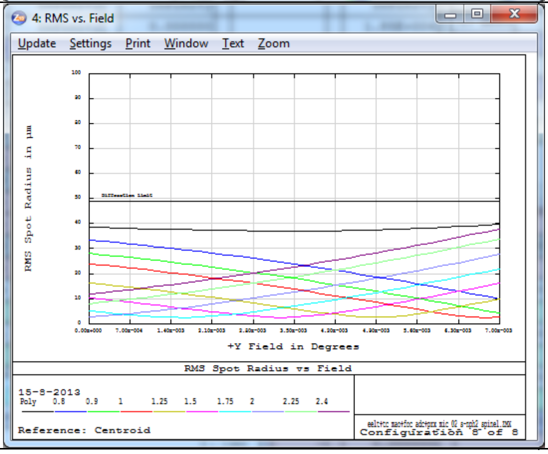

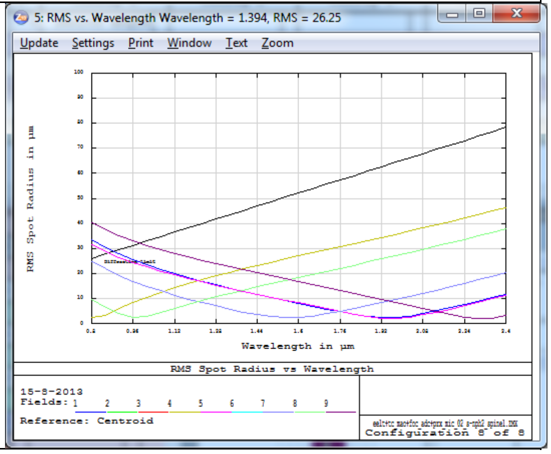

Counter rot. ADC (zero-dev.)

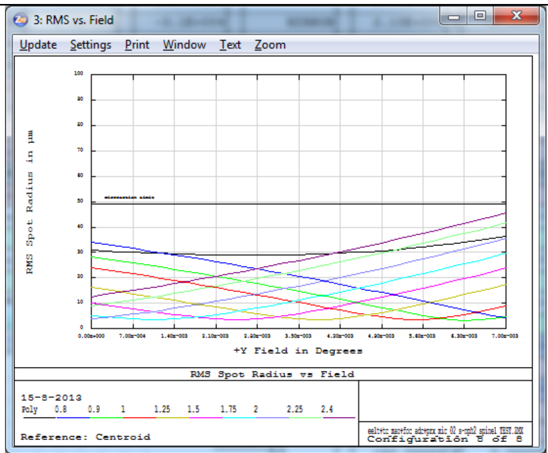

15-8-2013
Reference: Centroid
eelt+tc mao+foc adc+prx mic 02 s-opt2 spinel TEST.ZMX
Configuration 8 of 8

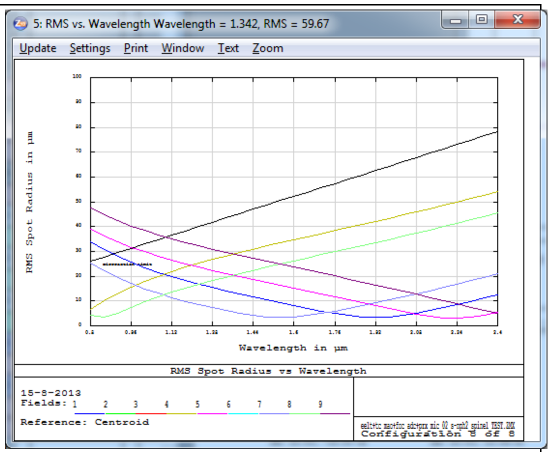

15-8-2013
Reference: Centroid
eelt+tc mao+foc adc+prx mic 02 s-opt2 spinel TEST.ZMX
Configuration 8 of 8

Linear ADC

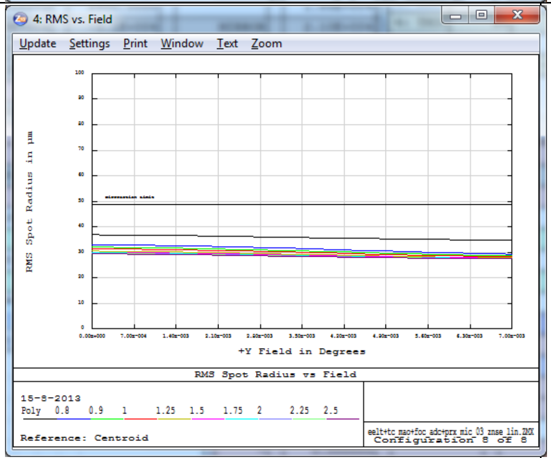

15-8-2013
Reference: Centroid
eelt+tc mao+foc adc+prx mic 03 zmse lin.ZMX
Configuration 8 of 8

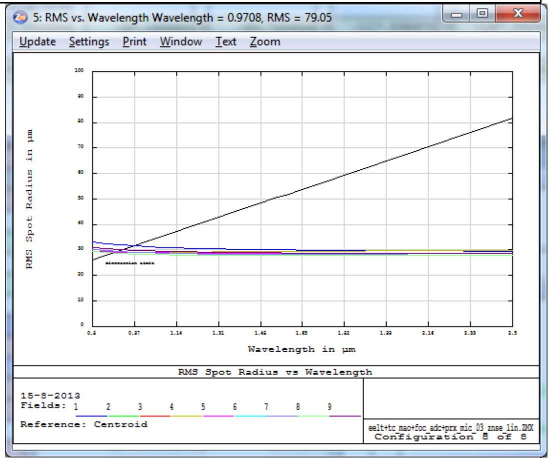

15-8-2013
Reference: Centroid
eelt+tc mao+foc adc+prx mic 03 zmse lin.ZMX
Configuration 8 of 8

Linear ADC (zero-dev.)

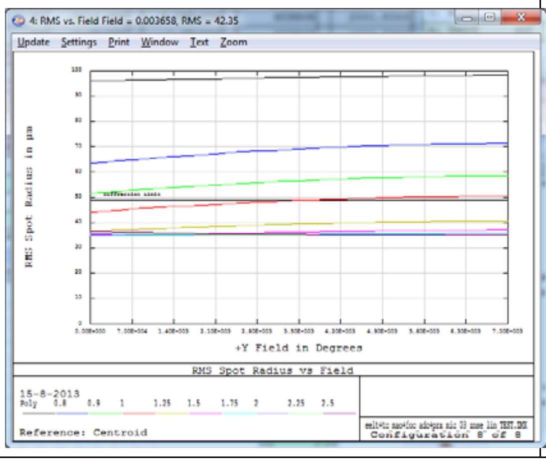

15-8-2013
Reference: Centroid
eelt+tc mao+foc adc+prx mic 03 zmse lin TEST.ZMX
Configuration 8 of 8

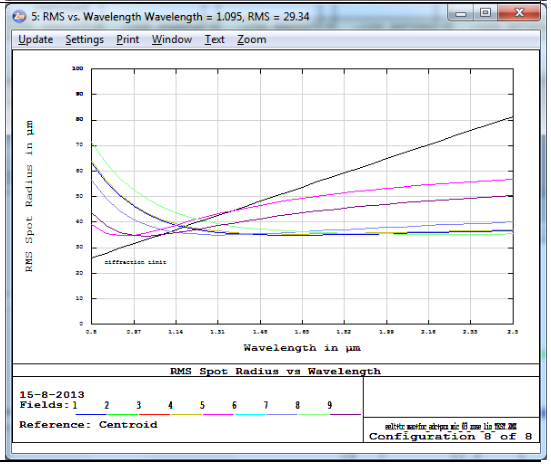

15-8-2013
Reference: Centroid
eelt+tc mao+foc adc+prx mic 03 zmse lin TEST.ZMX
Configuration 8 of 8

Linear ADC with fold mirror